

Factored-NeuS: Reconstructing Surfaces, Illumination, and Materials of Possibly Glossy Objects

Yue Fan¹ Ningjing Fan¹ Ivan Skorokhodov² Oleg Voynov^{3,4} Savva Ignatyev³
 Evgeny Burnaev^{3,4} Peter Wonka² Yiqun Wang^{1*}
¹Chongqing University ²KAUST ³Skoltech ⁴AIRI

Abstract

We develop a method that recovers the surface, materials, and illumination of a scene from its posed multi-view images. In contrast to prior work, it does not require any additional data and can handle glossy objects or bright lighting. It is a progressive inverse rendering approach, which consists of three stages. In the first stage, we reconstruct the scene radiance and signed distance function (SDF) with a novel regularization strategy for specular reflections. We propose to explain a pixel color using both surface and volume rendering jointly, which allows for handling complex view-dependent lighting effects for surface reconstruction. In the second stage, we distill light visibility and indirect illumination from the learned SDF and radiance field using learnable mapping functions. Finally, we design a method for estimating the ratio of incoming direct light reflected in a specular manner and use it to reconstruct the materials and direct illumination. Experimental results demonstrate that the proposed method outperforms the current state-of-the-art in recovering surfaces, materials, and lighting without relying on any additional data.

1. Introduction

Reconstructing shape, material, and lighting from multiple views has wide applications in computer vision, virtual reality, augmented reality, and shape analysis. The emergence of neural radiance fields [27] provides a framework for high-quality scene reconstruction. Subsequently, many works [11, 31, 42, 43, 49] have incorporated implicit neural surfaces into neural radiance fields, further enhancing the quality of surface reconstruction from multi-views. Recently, several works [29, 38, 53, 55, 56] have utilized coordinate-based networks to predict materials and learned parameters to represent illumination, followed by synthesizing image color using physically-based rendering equations to achieve material and lighting reconstruction. However, these meth-

ods typically do not fully consider the interdependence between different components, leading to the following issues with glossy surfaces when using real data.

First, surfaces with glossy materials typically result in highlights. The best current methods [11, 42, 43] for reconstructing implicit neural surfaces rarely consider material information and directly reconstruct surfaces. The surface parameters can then be frozen for subsequent material reconstruction. Since neural radiance fields typically model such inconsistent colors as bumpy surfaces as shown in Fig. 1 left, the artifacts from surface reconstruction will affect material reconstruction if surfaces and materials are reconstructed sequentially. Second, a glossy surface can affect the decomposition of the reflected radiance into a diffuse component and a specular component. Typically, the specular component leaks into the diffuse component, resulting in inaccurate modeling as shown in Fig. 1 right. Third, focusing on synthetic data makes it easier to incorporate complex physically-based rendering algorithms [5, 45], but they may not be robust enough to work on real data.

In this work, we consider the impact of glossy surfaces on surface and material reconstruction based on implicit representation. Although existing methods based on explicit representations, such as 3D Gaussian Splatting (3DGS) [20], have made progress in surface reconstruction [8, 16, 51] and inverse rendering [12, 18, 21, 24, 36], the unique advantages of implicit representations, such as low storage requirements and smooth surface modeling, still make them worthy of being explored as a separate research branch. This paper focuses solely on methods based on implicit representation and further extends research in reconstructing glossy objects. To better handle glossy surfaces, we jointly use surface and volume rendering. Volume rendering does not decompose the reflected radiance, while surface rendering considers the diffuse and specular radiance separately. The learned SDF network enables accurate radiance reconstruction in volume rendering while also being capable of providing correct surface information in surface rendering to model specular and diffuse components into directional and non-directional parts. Both work together to regularize accurate and ef-

*Corresponding author: yiqun.wang@cqu.edu.cn



Figure 1. Left: Geometry visualization for NeuS, Geo-NeuS and our method on the Pot scene from SK3D dataset. Existing surface reconstruction methods struggle to recover the correct geometry of glossy objects due to the complex view-dependent effects they induce. The weak color model of these methods compels to represent such effects through concave geometric deformations rather than proper view-dependent radiance, leading to shape artifacts. In contrast, our method can correctly reconstruct a highly reflective surface due to our joint appearance, diffuse, and specular color training strategy. Right: Visualization of the recovered diffuse color component on the Bunny scene from DTU for IndiSG [56] and our method. Existing inverse rendering methods overestimate the diffuse material component in the presence of specular highlights. Our regularization strategy allows us to properly disentangle the color into diffuse and specular components.

efficient SDF surface reconstruction of glossy objects. To better recover diffuse and specular components, we estimate the ratio of incoming light reflected in a specular manner. By introducing this parameter into a Spherical Gaussian representation of the BRDF for inverse rendering, we can better model the reflection of glossy surfaces and decompose more accurate diffuse albedo information. Furthermore, we propose predicting continuous light visibility for signed distance functions to further enhance the quality of reconstructed materials and illumination. Our experimental results have shown that our factorization of surface, materials, and illumination achieves state-of-the-art performance on both synthetic and real datasets.

We believe our approach outperforms recent work because it was developed primarily on real data. The fundamental challenge in material and lighting reconstruction is the lack of available ground truth information for real datasets. Our solution was to work with real data and improve surface reconstruction as our main metric by experimenting with different materials and lighting decompositions as a regularizer, indirectly measuring the success of material and lighting reconstruction through surface metrics. By contrast, most recent works [10, 53, 56] use surface reconstruction and real data more as an afterthought, focusing instead on increasingly complex material and lighting reconstruction with synthetic data. However, we believe that this typically does not translate as well to real data as our approach.

2. Related work

Neural radiance fields. NeRF [27] is a seminal work in 3D reconstruction. Important improvements were proposed by Mip-NeRF [1] and Mip-NeRF360 [2]. One line of work explores the combination of different data structures with MLPs, such as factored volumes [6, 7, 44] or voxels [28, 33, 34]. Multiple approaches take a step towards extending neural radiance fields to reconstruct material information [13, 14, 39, 47, 50].

Implicit neural surfaces. Implicit neural surfaces are typically represented by occupancy functions or signed distance fields (SDFs). Some early works [9, 26, 32] take point clouds

as input and output implicit neural surface representations. Many works have studied how to obtain implicit neural surfaces from images, initially focusing on surface rendering only [30, 48]. Subsequent methods followed NeRF to employ volume rendering, e.g. UNISURF [31], VolSDF [49], NeuS [42], HF-NeuS [43], and Geo-NeuS [11].

Joint reconstruction of surface, material, and illumination. Ideally, we would like to jointly reconstruct the 3D geometry, material properties, and lighting conditions of a scene from 2D images. Several methods employ strategies to simplify the problem such as assuming known lighting conditions (NeRV [37] and NeRD [3]) or pre-training (ENVIDR [23]). PhySG [53], NeRFactor [55], and NeROIC [22] use Spherical Gaussians, point light sources, and spherical harmonics, respectively, to decompose unknown lighting from a set of images. Using an illumination integration network, Neural-PIL [4] further reduces the computational cost of lighting integration. IRON [54] uses SDF-based volume rendering methods to obtain better geometric details in the shape recovery stage. NVDiffrec [29] explicitly extracts triangle mesh from tetrahedral representation for better material and lighting modeling. IndiSG [56] uses Spherical Gaussians to represent indirect illumination and achieves good lighting decomposition results. Some works [10, 19, 46, 52, 57] continue to improve the efficiency and quality of inverse rendering but do not consider cases with a glossy appearance. NeAI [58] proposes neural ambient illumination to enhance the rendering quality of glossy appearance. NeRO [25] highlights its good performance in reconstructing reflective objects. Ref-NeuS [13] learns specular reflection intensity and attenuates the impact of pixels affected by specular reflection. Despite a lot of recent activity in this area, existing frameworks still struggle to effectively reconstruct reflective or glossy surfaces, lighting, and material information directly from images, especially real-world captured images.

3. Method

Our framework has three training stages to gradually decompose the shape, materials, and illumination. The input to our

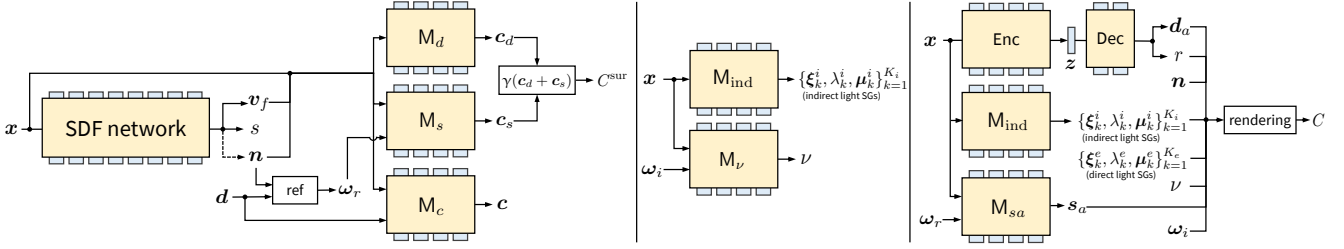


Figure 2. Overview for Stage 1 (left), Stage 2 (mid), and Stage 3 (right) training pipelines. The first stage (left) trains the SDF network S_θ which outputs a feature vector $\mathbf{v}_f \in \mathbb{R}^{256}$, SDF value $s \in \mathbb{R}$, and normal $\mathbf{n} \in \mathbb{S}^2$ (as a normalized gradient of s ; denoted via the dashed line); diffuse and specular surface color networks M_d and M_s produce their respective colors $\mathbf{c}_d, \mathbf{c}_s \in \mathbb{R}^3$ via surface rendering, which are then combined through tone mapping $\gamma(\cdot)$ to get the final surface color $C^{\text{sur}} \in \mathbb{R}^3$; volumetric color network M_c produces the volumetrically rendered color $C^{\text{vol}} \in \mathbb{R}^3$. The ref operation denotes computation of the reflection direction $\omega_r \in \mathbb{S}^2$ from normal \mathbf{n} and ray direction $\omega \in \mathbb{S}^2$. In the second stage (mid), indirect light network M_{ind} and light visibility network M_ν produce their respective indirect light SGs and light visibility ν . In the third stage (right), we optimize the material BRDF auto-encoder with the sparsity constraint [56], our novel specular albedo network M_{s_a} , and the indirect illumination network M_{ind} . See Sec 3 for details.

framework is a set of images. In the first stage, we reconstruct the surface from a (possibly glossy) appearance by jointly using volume rendering and surface rendering. After that, we use the reconstructed radiance field to extract direct illumination visibility and indirect illumination. In the final stage, we recover the direct illumination map and materials’ bidirectional reflectance distribution function (BRDF), proposing to use a BRDF with a learnable specular albedo.

3.1. Stage 1: Surface reconstruction from glossy appearance

Current inverse rendering methods first recover implicit neural surfaces, typically represented as SDFs, from multi-view images to recover shape information, then freeze the parameters of neural surfaces to further recover the material. However, this approach does not consider specular reflections that produce highlights and often models this inconsistent color as bumpy surface geometry as depicted in Fig. 1 left. This incorrect surface reconstruction has a negative impact on subsequent material reconstruction. We propose a neural surface reconstruction method that considers the appearance, diffuse color, and specular color of glossy surfaces at the same time, whose architecture is given in Fig. 2. Our inspiration comes from the following observations. First, according to GeoNeuS [11], using SDF point cloud supervision can make the colors of surface points and volume rendering more similar. We abandoned the idea of using additional surface points to supervise SDFs and directly used two different MLPs to predict the surface rendering and volume rendering results and narrow the gap between these two colors using network training. In addition, when modeling glossy surfaces, RefNeRF [39] proposes a method of decomposing reflected radiance into diffuse and specular components, which can better model the glossy appearance. However, this approach is unstable when directly applied to reconstruct implicit surfaces. We propose to simultaneously optimize the radiance from the volumetric rendering and the surface rendering. For surface rendering, we further split the reflected radiance into

a diffuse and a specular component. This can achieve an improved surface reconstruction of glossy surfaces.

Shape representation. We model shape as a signed distance function $S_\theta : \mathbf{x} \mapsto (s, \mathbf{v}_f)$, which maps a 3D point $\mathbf{x} \in \mathbb{R}^3$ to its signed distance value $s \in \mathbb{R}$ and a feature vector $\mathbf{v}_f \in \mathbb{R}^{256}$. SDF allows computing a normal \mathbf{n} directly by calculating the gradient: $\mathbf{n} = \nabla S_\theta(\mathbf{x}) / \|\nabla S_\theta(\mathbf{x})\|$.

Synthesize appearance. Learning implicit neural surfaces from multi-view images often requires synthesizing appearance/color to optimize the underlying surface. The recent use of volume rendering in NeuS [42] has been shown to better reconstruct surfaces. According to Eq. 14 in Appx A, the discretization formula for volume rendering is $C^{\text{vol}} = \sum_{i=1}^n T_i \alpha_i \mathbf{c}_i = \sum_{i=1}^n w_i \mathbf{c}_i$ with n sampled points $\{\mathbf{r}(t_i)\}_{i=1}^n$ on the ray, where $\alpha_i = \max(\Phi_s(S_\theta(\mathbf{r}(t_i))) - \Phi_s(S_\theta(\mathbf{r}(t_{i+1}))), \Phi_s(S_\theta(\mathbf{r}(t_i))), 0)$, which is discrete opacity values following NeuS, where $\Phi_s = 1/(1 + e^{-x})$ is a sigmoid function and $T_i = \prod_{j=1}^{i-1} (1 - \alpha_j)$ is the discrete transparency. Similar to the continuous case, we can also define discrete weights $w_i = T_i \alpha_i$. To compute color \mathbf{c}_i on the point $\mathbf{r}(t_i)$, we define a color mapping $M_c : (\mathbf{x}, \mathbf{n}, \mathbf{d}, \mathbf{v}_f) \mapsto \mathbf{c}$ from any 3D point \mathbf{x} given its feature vector \mathbf{v}_f , normal \mathbf{n} and ray direction \mathbf{d} .

Synthesize diffuse and specular components. We also synthesize separated diffuse and specular components as proposed in [15, 23, 50], but uniquely, we simultaneously preserve the synthesis of the overall appearance. This idea comes from surface rendering, which better handles surface reflections. From Eq. 16 in Appx A, the radiance L_o of surface point \mathbf{x} and outgoing viewing direction ω_o can be decomposed into two parts: diffuse and specular radiance.

$$L_o(\mathbf{x}, \omega_o) = \frac{d_a}{\pi} \int_{\Omega} L_i(\mathbf{x}, \omega_i) (\omega_i \cdot \mathbf{n}) d\omega_i \quad (1)$$

$$+ \int_{\Omega} f_s(\mathbf{x}, \omega_i, \omega_o) L_i(\mathbf{x}, \omega_i) (\omega_i \cdot \mathbf{n}) d\omega_i \quad (2)$$

$$= M_d(\mathbf{x}, \mathbf{n}) + M_s(\mathbf{x}, \omega_o, \mathbf{n}) \quad (3)$$

We define two neural networks to predict diffuse and spec-

ular components separately. We use the term diffuse radiance to refer to the component of the reflected radiance that stems from a diffuse surface reflection. We define a mapping $M_d : (\mathbf{x}, \mathbf{n}, \mathbf{v}_f) \mapsto \mathbf{c}_d$ for diffuse radiance that maps surface points \mathbf{x} , surface normals \mathbf{n} , and feature vectors \mathbf{v}_f to diffuse radiance. For simplicity, we assume that the diffuse radiance is not related to the outgoing viewing direction ω_o .

We use the term specular radiance to describe the non-diffuse (view-direction dependent) component of the reflected radiance. Ref-NeRF [39] proposes to model the glossy appearance using the reflection direction instead of the viewing one. However, from Eq. 3, we can observe that specular radiance is also highly dependent on the surface normal, which is particularly important when reconstructing SDF. In contrast to Ref-NeRF, we further condition specular radiance on the surface normal. Therefore, we define specular radiance $M_s : (\mathbf{x}, \omega_r, \mathbf{n}, \mathbf{v}_f) \mapsto \mathbf{c}_s$, which maps surface points \mathbf{x} , reflection direction ω_r , surface normals \mathbf{n} , and feature vectors \mathbf{v}_f to specular radiance, where $\omega_r = 2(\omega_o \cdot \mathbf{n})\mathbf{n} - \omega_o$.

Surface rendering focuses the rendering process on the surface, allowing for a better understanding of highlights on the surface compared to volume rendering, but requires calculating surface points. We sample n points on the ray $\{\mathbf{r}(t_i) | i = 1, \dots, n\}$. We query the sampled points to find the first point $\mathbf{r}(t'_i)$ whose SDF value is less than zero $S_\theta(\mathbf{r}(t'_i)) < 0$. Then the point $\mathbf{r}(t_{i'-1})$ sampled before $\mathbf{r}(t'_i)$ has the SDF value greater than or equal to zero $S_\theta(\mathbf{r}(t_{i'-1})) \geq 0$. To account for the possibility of rays interacting with objects and having multiple intersection points, we select the first point with a negative SDF value to solve this issue.

We use two neural networks to predict the diffuse radiance and specular radiance of two sampling points $\mathbf{r}(t_{i'-1})$ and $\mathbf{r}(t'_i)$. The diffuse radiance of the two points calculated by the diffuse network M_d will be $\mathbf{c}_d^{i'-1}$ and $\mathbf{c}_d^{i'}$. The specular radiance of the two points calculated by the specular network M_s will be $\mathbf{c}_s^{i'-1}$ and $\mathbf{c}_s^{i'}$. Therefore, the diffuse radiance and specular radiance of the surface point \mathbf{x} can be calculated as follows.

$$\mathbf{c}_d = M_d(\mathbf{x}, \mathbf{n}) = \frac{w_{i'-1}\mathbf{c}_d^{i'-1} + w'_i\mathbf{c}_d^{i'}}{w_{i'-1} + w'_i} \quad (4)$$

$$\mathbf{c}_s = M_s(\mathbf{x}, \omega_o, \mathbf{n}) = \frac{w_{i'-1}\mathbf{c}_s^{i'-1} + w'_i\mathbf{c}_s^{i'}}{w_{i'-1} + w'_i} \quad (5)$$

The final radiance of the intersection of the ray and the surface is calculated by a tone mapping:

$$\mathbf{c}^{\text{sur}} = \gamma(\mathbf{c}_d + \mathbf{c}_s) \quad (6)$$

where γ is a pre-defined tone mapping function that converts linear color to sRGB [39] while ensuring that the resulting color values are within the valid range of [0, 1].

Training strategies. In our training process, we define three loss functions, namely volume radiance loss \mathcal{L}_{vol} , surface radiance loss \mathcal{L}_{sur} , and regularization loss \mathcal{L}_{reg} . The volume radiance loss \mathcal{L}_{vol} is measured by calculating the \mathcal{L}_1 distance between the ground truth colors C^{gt} and the volume radiances C^{vol} of a subset of rays \mathcal{R} . The surface radiance loss \mathcal{L}_{sur} is measured by calculating the \mathcal{L}_1 distance between the ground truth colors C^{gt} and the surface radiances C^{sur} . \mathcal{L}_{reg} is an Eikonal loss term on the sampled points. We use weights λ_{sur} and λ_{reg} to balance the impact of these three losses. The overall training loss is as follows. See Appx C for details of training strategies.

$$\mathcal{L} = \mathcal{L}_{\text{vol}} + \lambda_{\text{sur}}\mathcal{L}_{\text{sur}} + \lambda_{\text{reg}}\mathcal{L}_{\text{reg}} \quad (7)$$

3.2. Stage 2: Learning direct lighting visibility and indirect illumination

At this stage, we focus on predicting the lighting visibility and indirect illumination of a surface point \mathbf{x} under different incoming light direction ω_i using the SDF in the first stage.

Visibility is an important factor in shadow computation. It calculates the visibility of the current surface point \mathbf{x} in the direction of the incoming light ω_i . Path tracing of the SDF is commonly used to obtain a binary visibility (0 or 1) as used in IndiSG [56], but this kind of visibility is not friendly to network learning. Inspired by NeRFactor [55], we propose to use an integral representation with the continuous weight function $w(t)$ (with a range from 0 to 1 and sourced from stage 1) for the SDF to express light visibility. Specifically, we establish a neural network $M_\nu : (\mathbf{x}, \omega_i) \mapsto \nu$, that maps the surface point \mathbf{x} and incoming light direction ω_i to visibility, and the ground truth value of light visibility is obtained by integrating the weights w_i of the SDF of sampling points along the incoming light direction and can be expressed as $\nu^{\text{gt}} = 1 - \sum_{i=1}^n w_i$.

Indirect illumination refers to the light that is reflected or emitted from surfaces in a scene and then illuminates other surfaces, rather than directly coming from a light source, which contributes to the realism of rendered images. Following IndiSG [56], we parameterize indirect illumination $I(\mathbf{x}, \omega_i)$ via $K_i = 24$ Spherical Gaussians (SGs). For more details, see Appx D.

3.3. Stage 3: Recovering materials and direct illumination

Reconstructing good materials and lighting from scenes with highlights is a challenging task. Following prior works [53, 56], we use the Ward BRDF model [45] and represent BRDF $f_s(\omega_i | \xi_s, \lambda_s, \mu_s)$ via Spherical Gaussians [53]. Direct (environment) illumination is represented using $K_e = 128$ SGs:

$$E(\mathbf{x}, \omega_i) = \sum_{k=1}^{K_e} E_k(\omega_i | \xi_k^e, \lambda_k^e, \mu_k^e) \quad (8)$$

and render diffuse radiance and specular radiance of direct illumination in a way similar to Eq. 2.

$$L_d(\mathbf{x}) = \frac{\mathbf{d}_a}{\pi} \sum_{k=1}^{K_e} (\nu(\mathbf{x}, \boldsymbol{\omega}_i) \otimes E_k(\boldsymbol{\omega}_i)) \cdot (\boldsymbol{\omega}_i \cdot \mathbf{n}) \quad (9)$$

$$L_s(\mathbf{x}, \boldsymbol{\omega}_o) = \sum_{k=1}^{K_e} (f_s^a \otimes \nu(\mathbf{x}, \boldsymbol{\omega}_i) \otimes E_k(\boldsymbol{\omega}_i)) \cdot (\boldsymbol{\omega}_i \cdot \mathbf{n}) \quad (10)$$

where \mathbf{d}_a is diffuse albedo.

To reconstruct a more accurate specular reflection effect, we use an additional neural network $M_{s_a} : (\mathbf{x}, \boldsymbol{\omega}_r) \mapsto \mathbf{s}_a \in [0, 1]$ to predict the specular albedo. The **modified** BRDF f_s^a is as follows:

$$f_s^a = \mathbf{s}_a \otimes f_s(\boldsymbol{\omega}_i; \boldsymbol{\xi}, \lambda, \boldsymbol{\mu}) = f_s(\boldsymbol{\omega}_i; \boldsymbol{\xi}, \lambda, \mathbf{s}_a \boldsymbol{\mu}) \quad (11)$$

For indirect illumination, the radiance is extracted directly from another surface and does not consider light visibility. The diffuse radiance and specular radiance of indirect illumination are as follows

$$L_d^{\text{ind}}(\mathbf{x}) = \frac{\mathbf{d}_a}{\pi} \sum_{k=1}^T I_k(\mathbf{x}, \boldsymbol{\omega}_i) \cdot (\boldsymbol{\omega}_i \cdot \mathbf{n}) \quad (12)$$

$$L_s^{\text{ind}}(\mathbf{x}, \boldsymbol{\omega}_o) = \sum_{k=1}^T (\mathbf{s}_a \otimes f_s) \otimes I_k(\mathbf{x}, \boldsymbol{\omega}_i) \cdot (\boldsymbol{\omega}_i \cdot \mathbf{n}) \quad (13)$$

Our final synthesized appearance is $C = L_d + L_s + L_d^{\text{ind}} + L_s^{\text{ind}}$ and supervised via an \mathcal{L}_1 RGB loss.

4. Experiments

4.1. Evaluation setup

Datasets. To evaluate the quality of surface reconstruction, we use the SK3D [40], DTU [17], Shiny [39], and Glossy [25] datasets. SK3D and DTU are two real-world captured datasets, while Shiny is synthetic. In the SK3D dataset, 100 views are provided for each scene. Compared to DTU, SK3D contains more reflective objects with complex view-dependent lighting effects. From SK3D, we select 4 glossy surface scenes with high levels of glare. For DTU, we select 4 scenes with high specularities to evaluate our method in terms of surface quality quantitatively and material decomposition qualitatively. The Shiny dataset has 5 different glossy objects rendered in Blender under conditions similar to the NeRF-synthetic dataset [27]. Glossy [25] dataset contains both real and synthetic scenes.

To evaluate the effectiveness of material and lighting reconstruction, we use the dataset provided by IndiSG [56], which has self-occlusion and complex materials. To evaluate the quality of material decomposition, the dataset also provides diffuse albedo, roughness, and masks for testing.

Baselines. Our main competitors are the methods that can also reconstruct all three scene properties: surface geometry, materials, and illumination. We choose NVDiffRec [29], PhysSG [53], and IndiSG [56] due to their popularity and availability of the source code. NVDiffRec uses tetrahedral marching to extract triangle meshes and obtains good material decomposition using a triangle-based renderer. PhysSG optimizes geometry and material information at the same time using a Spherical Gaussian representation for direct lighting and material. IndiSG first optimizes geometry and then uses a Spherical Gaussian representation for indirect lighting to improve the quality of material reconstruction.

Apart from that, we also compared against more general surface reconstruction methods to provide additional context for our results. For this, we use NeuS [42], Geo-NeuS [11], and NeRO [25]. NeuS is a popular implicit surface reconstruction method that achieves strong results without relying on extra data. Geo-NeuS improves upon NeuS by using additional point cloud supervision, obtained from structure from motion (SfM) [35]. NeRO is capable of reconstructing reflective objects effectively. In addition, we also compare with Ref-NeRF [39], which considers material decomposition, but due to modeling geometry using density function, it has difficulty extracting smooth geometry.

Evaluation metrics. We use the official evaluation protocol to compute Chamfer distance for the DTU dataset and also use Chamfer distance for the SK3D dataset. We utilize the PSNR metric, to quantitatively evaluate the quality of rendering, material, and illumination. We follow IndiSG [56] and employ masks to compute the PSNR metric in the foreground to evaluate the quality of materials and rendering. See Appx B for implementation details.

4.2. Surface reconstruction quality

We first demonstrate quantitative results in terms of Chamfer distance. We provide the numerical results for IndiSG, PhysSG, NeuS, Geo-NeuS, and NeRO for comparison. NVDiffrec struggles with glossy surface reconstruction as we subsequently verify qualitatively in Fig. 4. First, we list quantitative results on SK3D and DTU in Tab. 1. As shown in the table, our approach achieves the best and the second-best performance on the SK3D and DTU scenes with glossy surfaces. Geo-NeuS achieves better performance on the DTU dataset because the additional sparse 3D point clouds generated by structure from motion (SfM) for supervising the SDF network are accurate. Our approach can also incorporate the components of Geo-NeuS based on extra data, and the surface reconstruction quality will be further improved as shown in appendix F.2 (refer to it as Appx henceforth). However, on the SK3D scenes with more reflective surfaces, these sparse 3D points cannot be generated accurately by SfM, leading to poor surface reconstruction by Geo-NeuS. In contrast, our approach can reconstruct glossy surfaces on

Table 1. Quantitative results in terms of Chamfer distance on the scenes with high specularities on DTU [17] and SK3D [40]. Red and orange indicate the best and second-best algorithms. Geo-NeuS is separated because of the additional 3D point cloud (PC) for supervision. Our method achieves state-of-the-art surface reconstruction results on both glossy (this table) and regular (see Table 2) scenes.

	Pot	Funnel	Snowman	Jug	Mean	DTU 63	DTU 97	DTU 110	DTU 122	Mean
Geo-NeuS (PC) [11]	1.88	2.03	1.64	1.68	1.81	0.96	0.91	0.70	0.37	0.73
PhySG [53]	14.40	7.39	1.55	7.59	7.73	4.16	4.99	3.57	1.42	3.53
IndiSG [56]	5.62	4.05	1.74	2.35	3.44	1.15	2.07	2.60	0.61	1.61
NeuS [42]	2.09	3.93	1.40	1.81	2.31	1.01	1.21	1.14	0.54	0.98
NeRO [25]	6.03	2.63	1.71	4.23	3.65	1.32	1.47	1.14	0.57	1.12
Factored-NeuS (ours)	1.54	1.95	1.31	1.40	1.55	0.99	1.15	0.89	0.46	0.87

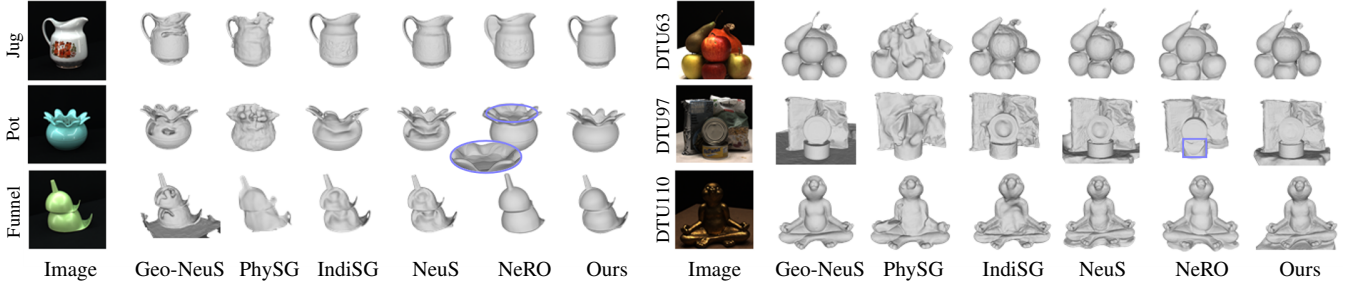


Figure 3. Qualitative results for DTU (left) and SK3D (right).

Table 2. Quantitative results in terms of Chamfer distance on DTU.

DTU	24	37	40	55	63	65	69	83
NeuS	1.00	1.37	0.93	0.43	1.01	0.65	0.57	1.48
NeRO	1.10	1.13	1.26	0.46	1.32	1.93	0.71	1.61
Ours	0.82	1.05	0.85	0.40	0.99	0.59	0.60	1.44
DTU	97	105	106	110	114	118	122	Mean
NeuS	1.21	0.83	0.52	1.14	0.35	0.49	0.54	0.83
NeRO	1.47	1.10	0.70	1.14	0.39	0.52	0.57	1.03
Ours	1.15	0.81	0.58	0.89	0.36	0.44	0.46	0.76

both SK3D and DTU without any explicit geometry information. IndiSG and PhySG share the same surface reconstruction method, but PhySG optimizes it together with the materials, while IndiSG freezes the underlying SDF after its initial optimization. Compared with IndiSG, PhySG cannot optimize geometry and material information well simultaneously on real-world acquired datasets with complex lighting and materials. We demonstrate large improvements over IndiSG and PhySG on both SK3D and DTU. NeRO focuses on highlight scenes, but our approach significantly outperforms it in both SK3D and DTU glossy scenes. Additional Chamfer distance comparisons for the other DTU scenes are in Tab. 2.

We further demonstrate the qualitative comparison results on glossy scenes from the SK3D and DTU datasets in Fig. 3. It can be seen that although Geo-NeuS has better quantitative evaluation metrics on DTU, it loses some of the fine details, such as the small dents on the metal can in DTU 97. By visualizing the results of the SK3D dataset, we can validate

that our method can reconstruct glossy surfaces without explicit geometric supervision. For NeRO, even in scenarios with a simple background and straightforward geometry, it still tends to lose certain details of the dataset and fills in shadowed areas (Pot and Jug). Furthermore, NeRO not only struggles to accurately restore detailed information but also fails to address the negative impact of partial highlights on geometry (DTU97). More DTU results are in Appx Fig. 10.

We further show qualitative results for surface reconstruction compared with NeuS, Ref-NeRF, IndiSG, PhySG, and NVDiffrec on the Shiny dataset, which is a synthetic dataset with glossy surfaces. From Fig. 4, we can observe that NeuS is easily affected by highlights, and the geometry reconstructed by Ref-NeRF has strong noise. PhySG is slightly better than IndiSG on the Shiny synthetic dataset with jointly optimizing materials and surfaces, such as toaster and car scenes, but still can not handle bright reflections. NeRO cannot accurately reconstruct the spoon in the coffee scene and performed poorly in the toaster bottom panel. The results of other scenarios in the Shiny dataset are shown in Appx Fig. 11. Our method can produce clean glossy surfaces without being affected by the issues caused by highlights. Overall, our approach demonstrates superior performance in surface reconstruction, especially on glossy surfaces. Additionally, we compare our method with Ref-NeuS [13] in Fig. 7. Ref-NeuS’s approach is easily affected by complex specular highlights, leading to suboptimal results on models in Shiny and SK3D with complex highlights.

For completeness, we also conducted experiments on the Glossy dataset [25], in which NeRO [25] excels. In

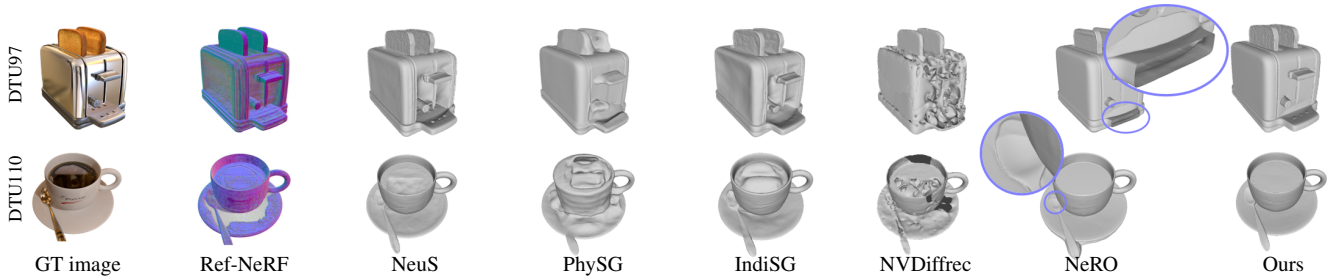


Figure 4. Qualitative results for the Shiny dataset(toaster and coffee).

Table 3. Quantitative PSNR results on IndiSG [56] dataset for IndiSG and our method. “SAI” refers to specular albedo improvement. Red and orange indicate the best and second-best algorithms.

	Balloons			Hotdog			Chair			Jugs			Mean		
	albedo	illumination	rendering												
PhySG	15.91	13.89	27.83	13.95	11.69	25.13	14.86	12.26	28.32	16.84	10.92	28.20	15.39	12.19	27.37
NVDiffrec	26.88	14.63	29.90	13.60	22.43	33.68	21.12	15.56	29.16	11.20	10.47	25.30	20.41	13.56	29.51
IndiSG	21.95	25.24	24.40	26.43	21.87	31.77	24.71	22.17	24.98	21.44	20.59	24.91	23.63	22.47	26.51
Ours w/o IndiLgt	23.13	18.24	29.45	25.62	17.97	35.97	25.22	18.04	34.31	22.87	21.84	26.30	24.21	19.02	31.51
Ours w/o SAI	24.09	25.97	28.82	30.58	23.50	36.05	25.23	22.13	32.64	19.64	20.40	33.56	24.89	23.00	32.77
Ours	25.79	21.79	33.89	30.72	20.23	36.71	26.33	20.97	34.58	22.94	21.84	36.48	26.28	21.21	35.41

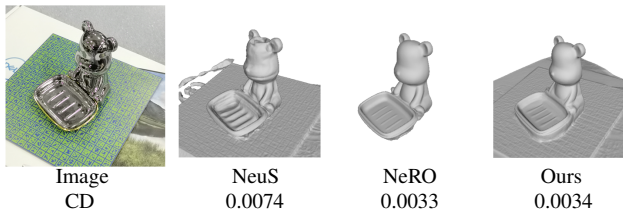


Figure 5. Qualitative results for Glossy dataset.

Fig. 5, we compared the reconstruction results of the bear scene with NeuS and NeRO, while other scenes are shown in Appx Fig. 12. It can be seen that our method and NeRO achieved comparable results on the Glossy dataset. Additional Chamfer distance metrics for the other scenes of the Glossy dataset are presented in Appx Tab. 5.

4.3. Material reconstruction and rendering quality

In Tab. 3, we evaluate the quantitative results in terms of PSNR metric for material and illumination reconstruction on the IndiSG dataset compared with PhySG, NVDiffrec, and IndiSG. For completeness, we also compare to the case where the specular albedo improvement was not used in Stage 3 (See in Eq. 11). Regarding diffuse albedo, although NVDiffrec showed a slight improvement over us in the balloons scene, we achieved a significant improvement over NVDiffrec in the other three scenes. Our method achieved the best results in material reconstruction. Moreover, our method achieves the best results in illumination quality without using the specular albedo improvement. Additionally, our method significantly outperforms other methods in terms of rendering quality and achieves better appearance synthesis results. We present the qualitative results of material reconstruction in Fig. 6, which shows that our method has better detail capture compared to IndiSG, PhySG, and NVDiffrec, such as the text on the balloon. Fig. 18 in Appx. also demonstrates the material decomposition effectiveness of our method on Shiny datasets with glossy surfaces.

In addition to the synthetic datasets with ground truth decomposed materials, we also provide qualitative results on real-world captured datasets (SK3D and DTU) in Appx Fig. 17 and show the effectiveness of material factorization. To offer a more detailed presentation of the reconstruction quality across continuous viewpoints, we include videos of diffuse albedo, indirect illumination, light visibility, and rendering for three different scenes in the supplementary materials. Furthermore, we perform relighting for these three scenes and provide videos to assess the relighting quality.

4.4. Ablation study

Surface reconstruction. To validate our surface reconstruction strategy in Stage 1, we selected the Pot scene from SK3D and ablated the method the following way. “ $\mathcal{L}_{vol} + \mathcal{L}_{sur}^I$ ” means that we only use volume rendering and surface rendering MLPs for surface reconstruction, without decomposing material information into diffuse and specular components. “ $\mathcal{L}_{vol} + \mathcal{L}_{vol}^{II}$ ” means we use two volume reconstructions where one of them is split into diffuse and specular components. Just using “ \mathcal{L}_{vol}^{II} ” like Ref-NeRF to split diffuse and specular components fails to reconstruct the correct surface due to inaccurate normal vectors in the reflection direction computation. We provide the quantitative (Chamfer distance) and qualitative results of different frameworks in Fig. ???. It can be seen that synchronizing the volume color and the color on the surface point has a certain effect in suppressing concavities, but still cannot meet the requirements for complex glossy surfaces with strong reflections. Using volume rendering to decompose diffuse and specular components can result in excessive influence from non-surface points, which still causes small concavities. When using our loss “ $\mathcal{L}_{vol} (\mathcal{L}_{vol}^I) + \mathcal{L}_{sur} (\mathcal{L}_{sur}^{II})$ ”, we can achieve reconstruction results without concavities. More qualitative results are shown in Appx Fig. 13.

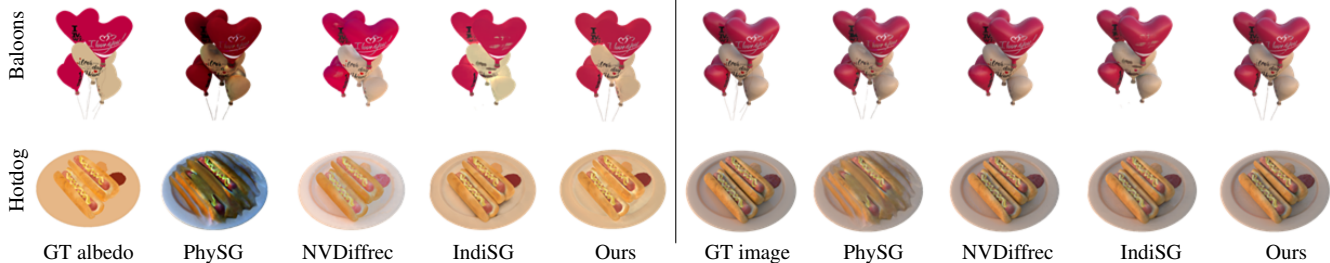


Figure 6. Qualitative results on IndiSG dataset (Balloons and Hotdog) in terms of albedo reconstruction (left) and rendering quality (right).



Figure 7. Comparison with Ref-NeuS.

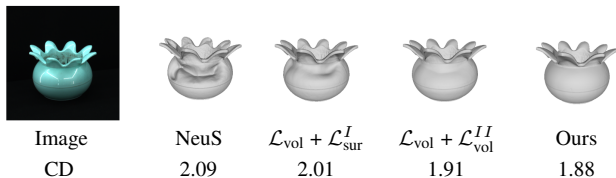


Figure 8. Ablation study for different reconstruction strategies.

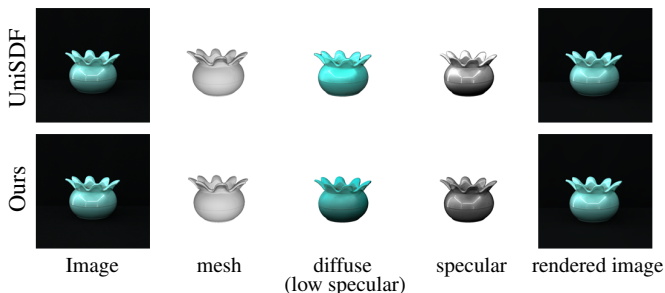


Figure 9. Comparison with UniSDF.

We also implement an ablation study on the concurrent work UniSDF [41] (coming code), which introduces a learnable parameter to weight the volume rendering (low-reflectance) and the specular component of volume rendering. We compared this method with ours and found that, although both approaches effectively decompose the surface, our diffuse (low-reflectance) component aligns more closely with reality with fewer specular components. This indicates that our method achieves a better decomposition.

Materials and illumination. We conduct an ablation study on the different components we proposed by evaluating their material and lighting performance on a complex scene, the hotdog, as shown in Tab. 4. “SI” refers to surface improvement, which means using networks to jointly synthesize volume color and decomposed surface color. “VI” stands for visibility improvement, which involves continuous light visibility supervision based on the SDF. “SAI” refers to specular albedo improvement, which incorporates specular albedo into the BRDF of Spherical Gaussians. We compare different settings in terms of diffuse albedo, roughness, appearance synthesis, and illumination. We use IndiSG as a reference and find that introducing volume rendering can

Table 4. Ablation study for materials and illumination decomposition in terms of PSNR. “Alb” is “diffuse albedo”, “Rough” is “roughness”, “Rend” is “appearance”, and “Illu” is “illumination”.

Method	Alb	Rough	Rend	Illu
IndiSG [56]	26.44	15.97	31.78	21.88
Ours w/o SAI w/o VI w/o SI	29.31	16.98	35.48	23.48
Ours w/o SAI w/o VI	29.64	17.86	36.36	23.41
Ours w/o SAI	30.58	18.83	36.05	23.50
Ours	30.76	23.10	36.71	20.24

improve the accuracy of material and lighting reconstruction. When the surface has no defects, further performing the surface improvement will enhance the quality of roughness and rendering but may cause a decrease in lighting reconstruction quality. Making the visibility supervision continuous improves the reconstruction of diffuse albedo, roughness, and lighting, but it also affects rendering quality. Introducing specular albedo can greatly improve roughness and rendering quality but negatively affect lighting reconstruction quality. We further show qualitative results in Appx Fig. 23 to highlight the importance of taking into account various factors, which enhance the reconstruction of materials and lighting. In stage 3, if we do not consider indirect illumination during the training process, the predicted results for rendering, material, and lighting will all experience a decline. The qualitative results are shown in Appx Fig. 24. The specific PSNR metrics can be found in Tab. 3

5. Conclusions

In this work, we propose Factored-NeuS, a novel approach to inverse rendering that factors geometry, material, and lighting from multiple views. Our first contribution is to simultaneously synthesize the appearance, diffuse radiance, and specular radiance during surface reconstruction. The combination of volume and decoupled surface rendering allows the geometry to be unaffected by glossy highlights. Our second contribution is to train networks to estimate reflectance albedo and learn a visibility function supervised by continuous values based on the SDF, so that our method is capable of better decomposing material and lighting. Experimental results show that our method surpasses the state-of-the-art in both geometry reconstruction quality and material reconstruction quality. A future research direction is how to effectively decompose materials for fine structures.

Acknowledgements

We would like to acknowledge support from the National Natural Science Foundation of China (62202076) and the KAUST - Center of Excellence for Generative AI, under award number 5940, and the NTGC-AI program.

References

- [1] Jonathan T Barron, Ben Mildenhall, Matthew Tancik, Peter Hedman, Ricardo Martin-Brualla, and Pratul P Srinivasan. Mip-nerf: A multiscale representation for anti-aliasing neural radiance fields. In *Proceedings of the IEEE/CVF International Conference on Computer Vision*, pages 5855–5864, 2021. 2
- [2] Jonathan T Barron, Ben Mildenhall, Dor Verbin, Pratul P Srinivasan, and Peter Hedman. Mip-nerf 360: Unbounded anti-aliased neural radiance fields. In *Proceedings of the IEEE/CVF Conference on Computer Vision and Pattern Recognition*, pages 5470–5479, 2022. 2
- [3] Mark Boss, Raphael Braun, Varun Jampani, Jonathan T Barron, Ce Liu, and Hendrik Lensch. Nerd: Neural reflectance decomposition from image collections. In *Proceedings of the IEEE/CVF International Conference on Computer Vision*, pages 12684–12694, 2021. 2
- [4] Mark Boss, Varun Jampani, Raphael Braun, Ce Liu, Jonathan Barron, and Hendrik Lensch. Neural-pil: Neural pre-integrated lighting for reflectance decomposition. *Advances in Neural Information Processing Systems*, 34:10691–10704, 2021. 2
- [5] Brent Burley and Walt Disney Animation Studios. Physically-based shading at disney. In *Acm Siggraph*, pages 1–7. vol. 2012, 2012. 1, 14
- [6] Eric R Chan, Connor Z Lin, Matthew A Chan, Koki Nagano, Boxiao Pan, Shalini De Mello, Orazio Gallo, Leonidas J Guibas, Jonathan Tremblay, Sameh Khamis, et al. Efficient geometry-aware 3d generative adversarial networks. In *Proceedings of the IEEE/CVF Conference on Computer Vision and Pattern Recognition*, pages 16123–16133, 2022. 2
- [7] Anpei Chen, Zexiang Xu, Andreas Geiger, Jingyi Yu, and Hao Su. Tensorf: Tensorial radiance fields. In *European Conference on Computer Vision (ECCV)*, 2022. 2
- [8] Danpeng Chen, Hai Li, Weicai Ye, Yifan Wang, Weijian Xie, Shangjin Zhai, Nan Wang, Haomin Liu, Hujun Bao, and Guofeng Zhang. Pgsr: Planar-based gaussian splatting for efficient and high-fidelity surface reconstruction. 2024. 1
- [9] Zhiqin Chen and Hao Zhang. Learning implicit fields for generative shape modeling. In *Proceedings of the IEEE/CVF Conference on Computer Vision and Pattern Recognition*, pages 5939–5948, 2019. 2
- [10] Youming Deng, Xueting Li, Sifei Liu, and Ming-Hsuan Yang. Dip: Differentiable interreflection-aware physics-based inverse rendering. *arXiv preprint arXiv:2212.04705*, 2022. 2
- [11] Qiancheng Fu, Qingshan Xu, Yew Soon Ong, and Wenbing Tao. Geo-neus: Geometry-consistent neural implicit surfaces learning for multi-view reconstruction. *Advances in Neural Information Processing Systems*, 35:3403–3416, 2022. 1, 2, 3, 5, 6, 13, 15
- [12] Jian Gao, Chun Gu, Youtian Lin, Hao Zhu, Xun Cao, Li Zhang, and Yao Yao. Relightable 3d gaussian: Real-time point cloud relighting with brdf decomposition and ray tracing. *arXiv:2311.16043*, 2023. 1
- [13] Wenhang Ge, Tao Hu, Haoyu Zhao, Shu Liu, and Ying-Cong Chen. Ref-neus: Ambiguity-reduced neural implicit surface learning for multi-view reconstruction with reflection. In *Proceedings of the IEEE/CVF International Conference on Computer Vision (ICCV)*, pages 4251–4260, 2023. 2, 6
- [14] Yuan-Chen Guo, Di Kang, Linchao Bao, Yu He, and Song-Hai Zhang. Nerfren: Neural radiance fields with reflections. In *Proceedings of the IEEE/CVF Conference on Computer Vision and Pattern Recognition*, pages 18409–18418, 2022. 2
- [15] Peter Hedman, Pratul P Srinivasan, Ben Mildenhall, Jonathan T Barron, and Paul Debevec. Baking neural radiance fields for real-time view synthesis. In *Proceedings of the IEEE/CVF international conference on computer vision*, pages 5875–5884, 2021. 3
- [16] Binbin Huang, Zehao Yu, Anpei Chen, Andreas Geiger, and Shenghua Gao. 2d gaussian splatting for geometrically accurate radiance fields. In *SIGGRAPH 2024 Conference Papers*. Association for Computing Machinery, 2024. 1
- [17] Rasmus Jensen, Anders Dahl, George Vogiatzis, Engin Tola, and Henrik Aanæs. Large scale multi-view stereopsis evaluation. In *Proceedings of the IEEE conference on computer vision and pattern recognition*, pages 406–413, 2014. 5, 6, 15
- [18] Yingwenqi Jiang, Jiadong Tu, Yuan Liu, Xifeng Gao, Xiaoxiao Long, Wenping Wang, and Yuexin Ma. Gaussianshader: 3d gaussian splatting with shading functions for reflective surfaces. In *Proceedings of the IEEE/CVF Conference on Computer Vision and Pattern Recognition*, pages 5322–5332, 2024. 1
- [19] Haiyan Jin, Isabella Liu, Peijia Xu, Xiaoshuai Zhang, Songfang Han, Sai Bi, Xiaowei Zhou, Zexiang Xu, and Hao Su. Tensorf: Tensorial inverse rendering. In *Proceedings of the IEEE/CVF Conference on Computer Vision and Pattern Recognition (CVPR)*, 2023. 2
- [20] Bernhard Kerbl, Georgios Kopanas, Thomas Leimkühler, and George Drettakis. 3d gaussian splatting for real-time radiance field rendering. *ACM Trans. Graph.*, 42(4):139–1, 2023. 1
- [21] Ye Keyang, Hou Qiming, and Zhou Kun. 3d gaussian splatting with deferred reflection. 2024. 1
- [22] Zhengfei Kuang, Kyle Olszewski, Menglei Chai, Zeng Huang, Panos Achlioptas, and Sergey Tulyakov. Neroic: neural rendering of objects from online image collections. *ACM Transactions on Graphics (TOG)*, 41(4):1–12, 2022. 2
- [23] Ruofan Liang, Huiting Chen, Chunlin Li, Fan Chen, Selvakumar Panneer, and Nandita Vijaykumar. Envidr: Implicit differentiable renderer with neural environment lighting. In *Proceedings of the IEEE/CVF International Conference on Computer Vision (ICCV)*, pages 79–89, 2023. 2, 3
- [24] Zhihao Liang, Qi Zhang, Ying Feng, Ying Shan, and Kui Jia. Gs-ir: 3d gaussian splatting for inverse rendering. In *Proceedings of the IEEE/CVF Conference on Computer Vision and Pattern Recognition*, pages 21644–21653, 2024. 1
- [25] Yuan Liu, Peng Wang, Cheng Lin, Xiaoxiao Long, Jiepeng Wang, Lingjie Liu, Taku Komura, and Wenping Wang. Nero:

- Neural geometry and brdf reconstruction of reflective objects from multiview images. *ACM Transactions on Graphics (TOG)*, 42(4):1–22, 2023. 2, 5, 6
- [26] Lars Mescheder, Michael Oechsle, Michael Niemeyer, Sebastian Nowozin, and Andreas Geiger. Occupancy networks: Learning 3d reconstruction in function space. In *Proceedings of the IEEE/CVF conference on computer vision and pattern recognition*, pages 4460–4470, 2019. 2
- [27] Ben Mildenhall, Pratul P Srinivasan, Matthew Tancik, Jonathan T Barron, Ravi Ramamoorthi, and Ren Ng. Nerf: Representing scenes as neural radiance fields for view synthesis. In *European conference on computer vision*, pages 405–421. Springer, 2020. 1, 2, 5
- [28] Thomas Müller, Alex Evans, Christoph Schied, and Alexander Keller. Instant neural graphics primitives with a multi-resolution hash encoding. *ACM Trans. Graph.*, 41(4):102:1–102:15, 2022. 2
- [29] Jacob Munkberg, Jon Hasselgren, Tianchang Shen, Jun Gao, Wenzheng Chen, Alex Evans, Thomas Müller, and Sanja Fidler. Extracting triangular 3d models, materials, and lighting from images. In *Proceedings of the IEEE/CVF Conference on Computer Vision and Pattern Recognition*, pages 8280–8290, 2022. 1, 2, 5
- [30] Michael Niemeyer, Lars Mescheder, Michael Oechsle, and Andreas Geiger. Differentiable volumetric rendering: Learning implicit 3d representations without 3d supervision. In *Proceedings of the IEEE/CVF Conference on Computer Vision and Pattern Recognition*, pages 3504–3515, 2020. 2
- [31] Michael Oechsle, Songyou Peng, and Andreas Geiger. Unisurf: Unifying neural implicit surfaces and radiance fields for multi-view reconstruction. In *Proceedings of the IEEE/CVF International Conference on Computer Vision*, pages 5589–5599, 2021. 1, 2
- [32] Jeong Joon Park, Peter Florence, Julian Straub, Richard Newcombe, and Steven Lovegrove. DeepSDF: Learning continuous signed distance functions for shape representation. In *Proceedings of the IEEE/CVF conference on computer vision and pattern recognition*, pages 165–174, 2019. 2
- [33] Christian Reiser, Songyou Peng, Yiyi Liao, and Andreas Geiger. Kilonerf: Speeding up neural radiance fields with thousands of tiny mlps. In *Proceedings of the IEEE/CVF International Conference on Computer Vision*, pages 14335–14345, 2021. 2
- [34] Sara Fridovich-Keil and Alex Yu, Matthew Tancik, Qinlong Chen, Benjamin Recht, and Angjoo Kanazawa. Plenoxels: Radiance fields without neural networks. In *CVPR*, 2022. 2
- [35] Johannes Lutz Schönberger and Jan-Michael Frahm. Structure-from-motion revisited. In *Conference on Computer Vision and Pattern Recognition (CVPR)*, 2016. 5
- [36] Yahao Shi, Yanmin Wu, Chenming Wu, Xing Liu, Chen Zhao, Haocheng Feng, Jingtuo Liu, Liangjun Zhang, Jian Zhang, Bin Zhou, et al. Gir: 3d gaussian inverse rendering for relightable scene factorization. *arXiv preprint arXiv:2312.05133*, 2023. 1
- [37] Pratul P Srinivasan, Boyang Deng, Xiuming Zhang, Matthew Tancik, Ben Mildenhall, and Jonathan T Barron. Nerv: Neural reflectance and visibility fields for relighting and view synthesis. In *Proceedings of the IEEE/CVF Conference on Computer Vision and Pattern Recognition*, pages 7495–7504, 2021. 2
- [38] Cheng Sun, Guangyan Cai, Zhengqin Li, Kai Yan, Cheng Zhang, Carl Marshall, Jia-Bin Huang, Shuang Zhao, and Zhao Dong. Neural-pbr reconstruction of shape, material, and illumination. In *Proceedings of the IEEE/CVF International Conference on Computer Vision*, pages 18046–18056, 2023. 1
- [39] Dor Verbin, Peter Hedman, Ben Mildenhall, Todd Zickler, Jonathan T Barron, and Pratul P Srinivasan. Ref-nerf: Structured view-dependent appearance for neural radiance fields. In *2022 IEEE/CVF Conference on Computer Vision and Pattern Recognition (CVPR)*, pages 5481–5490. IEEE, 2022. 2, 3, 4, 5, 16
- [40] Oleg Voynov, Gleb Bobrovskikh, Pavel Karpyshev, Andrei-Timotei Ardelean, Arseniy Bozhenko, Saveliy Galochkin, Ekaterina Karmanova, Pavel Kopanev, Yaroslav Labutin-Rymsho, Ruslan Rakhimov, et al. Multi-sensor large-scale dataset for multi-view 3d reconstruction. *arXiv preprint arXiv:2203.06111*, 2022. 5, 6
- [41] Fangjinhua Wang, Marie-Julie Rakotosaona, Michael Niemeyer, Richard Szeliski, Marc Pollefeys, and Federico Tombari. Unisdf: Unifying neural representations for high-fidelity 3d reconstruction of complex scenes with reflections. In *NeurIPS*, 2024. 8
- [42] Peng Wang, Lingjie Liu, Yuan Liu, Christian Theobalt, Taku Komura, and Wenping Wang. Neus: Learning neural implicit surfaces by volume rendering for multi-view reconstruction. *Advances in Neural Information Processing Systems*, 2021. 1, 2, 3, 5, 6, 12
- [43] Yiqun Wang, Ivan Skorokhodov, and Peter Wonka. Improved surface reconstruction using high-frequency details. *Advances in Neural Information Processing Systems*, 2022. 1, 2
- [44] Yiqun Wang, Ivan Skorokhodov, and Peter Wonka. Pet-neus: Positional encoding triplanes for neural surfaces. In *Proceedings of the IEEE/CVF Conference on Computer Vision and Pattern Recognition*, 2023. 2
- [45] Gregory J Ward. Measuring and modeling anisotropic reflection. In *Proceedings of the 19th annual conference on Computer graphics and interactive techniques*, pages 265–272, 1992. 1, 4, 14
- [46] Haoqian Wu, Zhipeng Hu, Lincheng Li, Yongqiang Zhang, Changjie Fan, and Xin Yu. Nefii: Inverse rendering for reflectance decomposition with near-field indirect illumination. In *Proceedings of the IEEE/CVF Conference on Computer Vision and Pattern Recognition (CVPR)*, pages 4295–4304, 2023. 2
- [47] Wenqi Yang, Guanying Chen, Chaofeng Chen, Zhenfang Chen, and Kwan-Yee K Wong. S³-nerf: Neural reflectance field from shading and shadow under a single viewpoint. *Advances in Neural Information Processing Systems*, 35:1568–1582, 2022. 2, 15
- [48] Lior Yariv, Yoni Kasten, Dror Moran, Meirav Galun, Matan Atzmon, Basri Ronen, and Yaron Lipman. Multiview neural surface reconstruction by disentangling geometry and appearance. *Advances in Neural Information Processing Systems*, 33:2492–2502, 2020. 2

- [49] Lior Yariv, Jiatao Gu, Yoni Kasten, and Yaron Lipman. Volume rendering of neural implicit surfaces. *Advances in Neural Information Processing Systems*, 34, 2021. [1](#), [2](#)
- [50] Lior Yariv, Peter Hedman, Christian Reiser, Dor Verbin, Pratul P Srinivasan, Richard Szeliski, Jonathan T Barron, and Ben Mildenhall. Baked sdf: Meshing neural sdf for real-time view synthesis. In *ACM SIGGRAPH 2023 Conference Proceedings*, pages 1–9, 2023. [2](#), [3](#)
- [51] Zehao Yu, Torsten Sattler, and Andreas Geiger. Gaussian opacity fields: Efficient adaptive surface reconstruction in unbounded scenes. *ACM Transactions on Graphics*, 2024. [1](#)
- [52] Jingyang Zhang, Yao Yao, Shiwei Li, Jingbo Liu, Tian Fang, David McKinnon, Yanghai Tsin, and Long Quan. Neif++: Inter-reflectable light fields for geometry and material estimation. In *International Conference on Computer Vision (ICCV)*, 2023. [2](#)
- [53] Kai Zhang, Fujun Luan, Qianqian Wang, Kavita Bala, and Noah Snavely. Physg: Inverse rendering with spherical gaussians for physics-based material editing and relighting. In *Proceedings of the IEEE/CVF Conference on Computer Vision and Pattern Recognition*, pages 5453–5462, 2021. [1](#), [2](#), [4](#), [5](#), [6](#)
- [54] Kai Zhang, Fujun Luan, Zhengqi Li, and Noah Snavely. Iron: Inverse rendering by optimizing neural sdf and materials from photometric images. In *Proceedings of the IEEE/CVF Conference on Computer Vision and Pattern Recognition*, pages 5565–5574, 2022. [2](#)
- [55] Xiuming Zhang, Pratul P Srinivasan, Boyang Deng, Paul Debevec, William T Freeman, and Jonathan T Barron. Nerfactor: Neural factorization of shape and reflectance under an unknown illumination. *ACM Transactions on Graphics (TOG)*, 40(6):1–18, 2021. [1](#), [2](#), [4](#), [13](#)
- [56] Yuanqing Zhang, Jiaming Sun, Xingyi He, Huan Fu, Rongfei Jia, and Xiaowei Zhou. Modeling indirect illumination for inverse rendering. In *Proceedings of the IEEE/CVF Conference on Computer Vision and Pattern Recognition*, pages 18643–18652, 2022. [1](#), [2](#), [3](#), [4](#), [5](#), [6](#), [7](#), [8](#), [12](#), [13](#)
- [57] Youjia Zhang, Teng Xu, Junqing Yu, Yuteng Ye, Yanqing Jing, Junle Wang, Jingyi Yu, and Wei Yang. Nemf: Inverse volume rendering with neural microflake field. In *Proceedings of the IEEE/CVF International Conference on Computer Vision (ICCV)*, pages 22919–22929, 2023. [2](#)
- [58] Yiyu Zhuang, Qi Zhang, Xuan Wang, Hao Zhu, Ying Feng, Xiaoyu Li, Ying Shan, and Xun Cao. Neai: A pre-convoluted representation for plug-and-play neural ambient illumination. *arXiv preprint arXiv:2304.08757*, 2023. [2](#)

A. Preliminaries

Volume rendering. The radiance C of the pixel corresponding to a given ray $\mathbf{r}(t) = \mathbf{o} + t\mathbf{d}$ at the origin $\mathbf{o} \in \mathbb{R}^3$ towards direction $\mathbf{d} \in \mathbb{S}^2$ is calculated using the volume rendering equation, which involves an integral along the ray with boundaries t_n and t_f (t_n and t_f are parameters to define the near and far clipping plane). This calculation requires the knowledge of the volume density σ and directional color \mathbf{c} for each point within the volume.

$$C(\mathbf{r}) = \int_{t_n}^{t_f} T(t)\sigma(\mathbf{r}(t))\mathbf{c}(\mathbf{r}(t), \mathbf{d})dt \quad (14)$$

The volume density σ is used to calculate the accumulated transmittance $T(t)$:

$$T(t) = \exp\left(-\int_{t_n}^{t_f} \sigma(\mathbf{r}_s)ds\right) \quad (15)$$

It is then used to compute a weighting function $w(t) = T(t)\sigma(\mathbf{r}(t))$ to weigh the sampled colors along the ray $\mathbf{r}(t)$ to integrate into radiance $C(\mathbf{r})$.

Surface rendering. The radiance $L_o(\mathbf{x}, \boldsymbol{\omega}_o)$ reflected from a surface point \mathbf{x} in direction $\boldsymbol{\omega}_o = -\mathbf{d}$ is an integral of bidirectional reflectance distribution function (BRDF) and illumination over half sphere Ω , centered at normal \mathbf{n} of the surface point \mathbf{x} :

$$L_o(\mathbf{x}, \boldsymbol{\omega}_o) = \int_{\Omega} L_i(\mathbf{x}, \boldsymbol{\omega}_i)f_r(\mathbf{x}, \boldsymbol{\omega}_i, \boldsymbol{\omega}_o)(\boldsymbol{\omega}_i \cdot \mathbf{n})d\boldsymbol{\omega}_i \quad (16)$$

where $L_i(\mathbf{x}, \boldsymbol{\omega}_i)$ is the illumination on \mathbf{x} from the incoming light direction $\boldsymbol{\omega}_i$, and f_r is BRDF, which is the proportion of light reflected from direction $\boldsymbol{\omega}_i$ towards direction $\boldsymbol{\omega}_o$ at the point \mathbf{x} .

B. Implementation details

Our full model is composed of several MLP networks, each one of them having a width of 256 hidden units unless otherwise stated. In Stage 1, the SDF network S_θ is composed of 8 layers and includes a skip connection at the 4-th layer, similar to NeuS [42]. The input 3D coordinate \mathbf{x} is encoded using positional encoding with 6 frequency scales. The diffuse color network M_d utilizes a 4-layer MLP, while the input surface normal \mathbf{n} is positional-encoded using 4 scales. For the specular color network M_s , a 4-layer MLP is employed, and the reflection direction $\boldsymbol{\omega}_r$ is also positional-encoded using 4 frequency scales. In the first stage, we exclusively focus on decomposing the highlight (largely white) areas. To reduce the complexity of considering color, we assume that the specular radiance is in grayscale and only consider changes in brightness. We can incorporate color information in later stages to obtain a more detailed specular reflection model. Like NeuS, the background is modeled by NeRF++.

In Stage 2, the light visibility network M_ν has 4 layers. To better encode the input 3D coordinate \mathbf{x} , positional encoding with 10 frequency scales is utilized. The input view direction $\boldsymbol{\omega}_i$ is also positional-encoded using 4 scales. The indirect light network M_{ind} in stage 2 comprises 4 layers.

In stage 3, the encoder part of the BRDF network consists of 4 layers, and the input 3D coordinate is positional-encoded using 10 scales. The output latent vector \mathbf{z} has 32 dimensions, and we impose a sparsity constraint on the latent code \mathbf{z} , following IndiSG [56]. The decoder part of the BRDF network is a 2-layer MLP with a width of 128, and the output has 4 dimensions, including the diffuse albedo $\mathbf{d}_a \in \mathbb{R}^3$ and roughness $r \in \mathbb{R}$. Finally, the specular albedo network M_{sa} uses a 4-layer MLP, where the input 3D coordinate \mathbf{x} is positional-encoded using 10 scales, and the input reflection direction $\boldsymbol{\omega}_r$ is positional-encoded using 4 scales.

The learning rate for all three stages begins with a linear warm-up from 0 to 5×10^{-4} during the first 5K iterations. It is controlled by the cosine decay schedule until it reaches the minimum learning rate of 2.5×10^{-5} , which is similar to NeuS. The weights λ_{sur} for the surface color loss are set for 0.1, 0.6, 0.6, 0.6 and 0.01 for DTU, SK3D, Shiny, Glossy, and the IndiSG dataset, respectively. For all datasets, the Fresnel value f in the rendering equation is set to 0.02. We train our model for 300K iterations in the first stage, which takes 11 hours in total. For the second and third stages, we train for 40K iterations, taking around 1 hour each. The training was performed on a single NVIDIA RTX 4090 GPU.

C. Training strategies of stage 1

In our training process, we define three loss functions, namely volume radiance loss \mathcal{L}_{vol} , surface radiance loss \mathcal{L}_{sur} , and regularization loss \mathcal{L}_{reg} . The volume radiance loss \mathcal{L}_{vol} is measured by calculating the \mathcal{L}_1 distance between the ground truth colors C^{gt} and the volume radiances C^{vol} of a subset of rays \mathcal{R} , which is defined as follows.

$$\mathcal{L}_{\text{vol}} = \frac{1}{|\mathcal{R}|} \sum_{\mathbf{r} \in \mathcal{R}} \|C_{\mathbf{r}}^{\text{vol}} - C_{\mathbf{r}}^{\text{gt}}\|_1 \quad (17)$$

The surface radiance loss \mathcal{L}_{sur} is measured by calculating the \mathcal{L}_1 distance between the ground truth colors C^{gt} and the surface radiances C^{sur} . During the training process, only a few rays have intersection points with the surface. We only care about the set of selected rays \mathcal{R}' , which satisfies the condition that each ray exists point whose SDF value is less than zero and not the first sampled point. The loss is defined as follows.

$$\mathcal{L}_{\text{sur}} = \frac{1}{|\mathcal{R}'|} \sum_{\mathbf{r} \in \mathcal{R}'} \|C_{\mathbf{r}}^{\text{sur}} - C_{\mathbf{r}}^{\text{gt}}\|_1 \quad (18)$$

\mathcal{L}_{reg} is an Eikonal loss term on the sampled points. Eikonal loss is a regularization loss applied to a set of sampling points

X , which is used to constrain the noise in signed distance function (SDF) generation.

$$\mathcal{L}_{\text{reg}} = \frac{1}{|\mathcal{X}|} \sum_{\mathbf{x} \in \mathcal{X}} (\|\nabla S_{\theta}(\mathbf{x})\|_2 - 1)^2 \quad (19)$$

We use weights λ_{sur} and λ_{reg} to balance the impact of these three losses. The overall training weights are as follows.

$$\mathcal{L} = \mathcal{L}_{\text{vol}} + \lambda_{\text{sur}} \mathcal{L}_{\text{sur}} + \lambda_{\text{reg}} \mathcal{L}_{\text{reg}} \quad (20)$$

D. Details of stage 2

At this stage, we focus on predicting the lighting visibility and indirect illumination of a surface point \mathbf{x} under different incoming light direction ω_i using the SDF in the first stage. Therefore, we need first to calculate the position of the surface point \mathbf{x} . In stage one, we have calculated two sampling points $\mathbf{r}(t_{i'-1}), \mathbf{r}(t'_i)$ near the surface. As Geo-NeuS [11], we weigh these two sampling points to obtain a surface point \mathbf{x} as follows.

$$\mathbf{x} = \frac{S_{\theta}(\mathbf{r}(t_{i'-1}))\mathbf{r}(t'_i) - S_{\theta}(\mathbf{r}(t'_i))\mathbf{r}(t_{i'-1})}{S_{\theta}(\mathbf{r}(t_{i'-1})) - S_{\theta}(\mathbf{r}(t'_i))} \quad (21)$$

Learning lighting visibility. Visibility is an important factor in shadow computation. It calculates the visibility of the current surface point \mathbf{x} in the direction of the incoming light ω_i . Path tracing of the SDF is commonly used to obtain a binary visibility (0 or 1) as used in IndiSG [56], but this kind of visibility is not friendly to network learning. Inspired by NeRFactor [55], we propose to use an integral representation with the continuous weight function $w(t)$ (from 0 to 1) for the SDF to express light visibility. Specifically, we establish a neural network $M_{\nu} : (\mathbf{x}, \omega_i) \mapsto \nu$, that maps the surface point \mathbf{x} and incoming light direction ω_i to visibility, and the ground truth value of light visibility is obtained by integrating the weights w_i of the SDF of sampling points along the incoming light direction and can be expressed as follows.

$$\nu^{gt} = 1 - \sum_{i=1}^n w_i \quad (22)$$

The weights of the light visibility network are optimized by minimizing the loss between the calculated ground truth values and the predicted values of a set of sampled incoming light directions $\Omega_i \subset \mathbb{S}^2$. This pre-integrated technique can reduce the computational burden caused by the integration for subsequent training.

$$\mathcal{L}_{\text{vis}} = \frac{1}{|\Omega_i|} \sum_{\omega \in \Omega_i} \|\nu_{\omega} - \nu_{\omega}^{gt}\|_1 \quad (23)$$

Learning indirect illumination. Indirect illumination refers to the light that is reflected or emitted from surfaces in a

scene and then illuminates other surfaces, rather than directly coming from a light source, which contributes to the realism of rendered images. Following IndiSG [56], we parameterize indirect illumination $I(\mathbf{x}, \omega_i)$ via $K_i = 24$ Spherical Gaussians (SGs) as follows.

$$I(\mathbf{x}, \omega_i) = \sum_{k=1}^{K_i} I_k(\omega_i | \xi_k^i(\mathbf{x}), \lambda_k^i(\mathbf{x}), \mu_k^i(\mathbf{x})) \quad (24)$$

where $\xi_k^i(\mathbf{x}) \in \mathbb{S}^2$, $\lambda_k^i(\mathbf{x}) \in \mathbb{R}_+$, and $\mu_k^i(\mathbf{x}) \in \mathbb{R}^3$ are the lobe axis, sharpness, and amplitude of the k -th Spherical Gaussian, respectively. For this, we train a network $M_{\text{ind}} : \mathbf{x} \mapsto \{\xi_k^i, \lambda_k^i, \mu_k^i\}_{k=1}^{K_i}$ that maps the surface point \mathbf{x} to the parameters of indirect light SGs. Similar to learning visibility, we randomly sample several directions ω_i from the surface point \mathbf{x} to obtain (pseudo) ground truth $I^{\text{gt}}(\mathbf{x}, \omega_i)$. Some of these rays have intersections \mathbf{x}' with other surfaces, thus, ω_i is the direction pointing from \mathbf{x} to \mathbf{x}' . We query our proposed color network M_c to get the (pseudo) ground truth indirect radiance $I^{\text{gt}}(\mathbf{x}, \omega_i)$ as follows.

$$I^{\text{gt}}(\mathbf{x}, \omega_i) = M_c(\mathbf{x}', \mathbf{n}', \omega_i, \mathbf{v}_f) \quad (25)$$

where \mathbf{n}' is the normal on the point \mathbf{x}' . We also use \mathcal{L}_1 loss to train the network.

$$\mathcal{L}_{\text{ind}} = \frac{1}{|M|} \sum_{m \in M} \|I(\mathbf{x}, \omega_m) - I_m^{\text{gt}}(\mathbf{x}, \omega_m)\|_1 \quad (26)$$

E. Details of stage 3

The combination of light visibility and illumination SG is achieved by applying a ratio to the lobe amplitude of the output SG, while preserving the center position of the SG. We randomly sample $K_s = 32$ directions within the SG lobe and compute a weighted average of the visibility with different directions.

$$\begin{aligned} & \nu(\mathbf{x}, \omega_i) \otimes E_k(\omega_i | \xi_k^e, \lambda_k^e, \mu_k^e) \\ & \approx E_k(\omega_i | \xi_k^e, \lambda_k^e, \frac{\sum_{s=1}^{K_s} E_k(\omega_s) \nu(\mathbf{x}, \omega_s)}{\sum_{s=1}^{K_s} E_k(\omega_s)} \mu_k^e) \end{aligned} \quad (27)$$

Here, we offer intuitive explanations for why the incorporation of specular albedo in the model results in a decrease in lighting prediction. The increase in the model's complexity is the primary reason. Specular albedo introduces a more detailed modeling of surface reflection characteristics, requiring additional parameters and learning capacity. This raises the difficulty of training the model, potentially resulting in overfitting or training instability, thereby affecting the accurate prediction of lighting.

F. Additional results

F.1. Additional results for the main text

We conduct a more in-depth comparison of our method with the already published work NeRO. For DTU datasets, our findings demonstrate that NeRO performs less effectively than our approach on real datasets DTU, especially in the regular scenes of DTU shown in Fig. 10. NeRO fails to address the negative impact of partial highlights on the geometry. For example, the highlighted region of the skull model is reconstructed as overly flat, while the Buddha model loses numerous details that should have been retained. Similar issues are also observed in the two plush toy scenes. Moreover, the presence of shadows causes NeRO to mistakenly reconstruct shadowed areas as real objects and fill them in (bricks and skull models). Fig. 11 shows three other scenes (helmet, teapot, and car) from the Shiny dataset. We have demonstrated that our method performs better than other methods on the Shiny dataset. NeRO exhibits defects in the dents and highlights of the helmet, as well as in the wheels of the car. Furthermore, we extend our comparison to include more scenes in the glossy dataset in Fig. 12 and Tab. 5, where although NeRO performs better, our method is also capable of mitigating the impact of highlights on geometry. Our method demonstrates comparable results to NeRO. Moreover, compared to NeuS, the results show a significant improvement. Note that the real datasets include bear, bunny, coral, and vase. The rest of the others are synthetic. As for material representation, we adopted the spherical Gaussians to represent the Ward BRDF model [45], while NeRO uses the spherical harmonics to represent the Disney BRDF model [5]. Tab. 6 and Fig. 14 show that we outperform NeRO in materials and rendering.

In order to prove the effectiveness of the combination of volume rendering and decoupled surface rendering, in Fig. 13, we additionally present the qualitative evaluation for more objects. It is evident that surface rendering is essential for decomposing diffuse and specular components, ensuring smooth reconstruction of glossy surfaces with complex reflections.

Fig. 15 illustrates the qualitative results of material reconstruction on the other scenes of the IndiSG dataset, highlighting the effectiveness of our method. For completeness, we visualize the decomposition of diffuse and specular in the first stage in Fig. 16. In the first stage, the decomposition of diffuse and specular is not a true BRDF model. This is because the MLP in the first stage is used solely for predicting the components of diffuse and specular reflection, rather than predicting material properties such as albedo and roughness. The decision to directly predict colors instead of material properties in the first stage serves two purposes: reducing model complexity by focusing on the direct prediction of specular reflection color, and optimizing geometry for bet-

ter reconstruction. By decomposing highlights through the network in the first stage, surfaces with specular reflections can be reconstructed more effectively, demonstrated by the presence of flower pot ablation, and without encountering the concavity issues observed in other methods.

In Fig. 17, from the DTU data, we can observe that our method can separate the specular reflection component from the diffuse reflection component, as seen in the highlights on the apple, can, and golden rabbit. Even when faced with a higher intensity of specular reflection, as demonstrated in the example showcased in SK3D, our method excels at preserving the original color in the diffuse part and accurately separating highlights into the specular part.

In Fig. 18, we show the diffuse albedo and rendering results of NVDiffrec, IndiSG, and our method. The rendering results indicate that our method can restore the original appearance with specular highlights more accurately, such as the reflections on the helmet and toaster compared to the IndiSG and NVDiffrec methods. The material reconstruction results show that our diffuse albedo contains less specular reflection information compared to other methods, indicating our method has a better ability to suppress decomposition ambiguity caused by specular highlights.

Additionally, in Fig. 19, Fig. 20, and Fig. 21, we presented all components, the rendering, albedo, roughness, diffuse color, specular color, light visibility, indirect light, and environment light results for the IndiSG, DTU and SK3D datasets, respectively. An interesting observation is that our reconstructed environment maps have the capability to represent multiple direct light illuminants, as demonstrated in the DTU dataset.

In Fig. 22, we additionally showcase the visualization results of relighting compared with the IndiSG method. IndiSG and ours yield different predictions for material, resulting in variations in the relighting results, but the relighting results generated by our method exhibit richer details. Our method demonstrates the practical utility employed in the relighting scenarios.

In Fig. 23, we show that introducing specular albedo also makes the sausage appear smoother and closer to its true color roughness, represented by black. In terms of lighting, when not using specular albedo, the lighting reconstruction achieves the best result, indicating a clearer reconstruction of ambient illumination. In summary, our ablation study highlights the importance of taking into account various factors when reconstructing materials and illumination from images. By evaluating the performance of different modules, we can better understand their role in improving the reconstruction quality.

In stage 3, if we do not consider indirect illumination during the training process, the predicted results for rendering, material, and lighting will all experience a decline. The qualitative results are shown in Fig. 24.

Table 5. Comparison with NeRO and NeuS on Glossy dataset.

Glossy	bear	bunny	coral	maneki	vase	angel	bell	cat	horse	luyu	potion	tbell	teapot	mean
NeuS	0.0074	0.0022	0.0016	0.0091	0.0101	0.0035	0.0146	0.0278	0.0053	0.0066	0.0393	0.0348	0.0546	0.0167
NeRO	0.0033	0.0012	0.0014	0.0024	0.0011	0.0034	0.0032	0.0044	0.0049	0.0054	0.0053	0.0035	0.0037	0.0033
Ours	0.0034	0.0017	0.0014	0.0027	0.0023	0.0034	0.0054	0.0059	0.0052	0.0060	0.0058	0.0035	0.0105	0.0044

Table 6. Comparison of material rendering on IndiSG dataset.

	Baloons			Hotdog		
	albedo	rough	render	albedo	rough	render
NeRO	14.65	18.91	23.84	11.54	18.42	26.95
Ours	25.79	19.75	33.89	30.72	23.10	36.71

F.2. Additional experiments

To have a fair comparison with Geo-NeuS on the DTU dataset, we incorporate the components of Geo-NeuS based on the additional data (the point clouds from SfM and image pairs) used in Geo-NeuS into our method. As shown in Tab. 7, our approach can further enhance the surface reconstruction quality on datasets where highlights are less pronounced.

Table 7. Quantitative results in terms of Chamfer distance on DTU [17].

	DTU 63	DTU 97	DTU 110	Mean
Geo-NeuS [11]	0.96	0.91	0.70	0.86
Factored-NeuS (ours)	0.99	1.15	0.89	1.01
Factored-NeuS (ours w/ Geo)	0.95	0.89	0.69	0.84

We conduct another experiment to compare our modeling approach with Ref-NeRF and S^3 -NeRF [47]. The experimental quantitative and qualitative results are shown in Fig. 25. Ref-NeRF utilizes volume rendering colors for diffuse and specular components. If we directly combine SDF and the architecture of Ref-NeRF, it is challenging to eliminate the influence of highlights. Furthermore, if we applied the construction method of S^3 -NeRF, which involves integrating surface rendering colors into volume rendering, to modify our model structure, we found that this modeling approach cannot address the issue of geometric concavity caused by highlights.

For chrome-like materials, We increase the Fresnel value to 0.75 in the rendering formula of stage 3 to test the impact of this operation. We show the results and their PSNR value in Fig. 26, we observed that increasing the Fresnel value indeed leads to the better reconstruction of objects with chrome-like materials. For the Toaster model, we observed a significant improvement in PSNR with an increased Fresnel value. However, we also noticed that solely increasing the

Fresnel value can result in the degradation of texture details. For instance, in the Coffee model, although the highlights on the spoon are better reconstructed, the text on the cup deteriorates. One of our future directions is to address this issue more effectively.

G. Limitations

In certain scenarios, our method still faces difficulties. For mesh reconstruction, despite improvements on the glossy parts in the DTU 97 tin model, the overall Chamfer distance does not significantly decrease due to the small proportion of glossy parts. However, for scenes with large areas of glossy parts, such as the flower pot model, our improvements are more pronounced and surpass Geo-NeuS. As seen in Appx Fig. 15, the reconstructed albedo of the chair still lacks some detail. The nails on the chair and the textures on the pillow are not accurately captured in the reconstructed geometry. A future research direction is how to effectively decompose materials for fine structures, such as nails on the backrest of a chair.

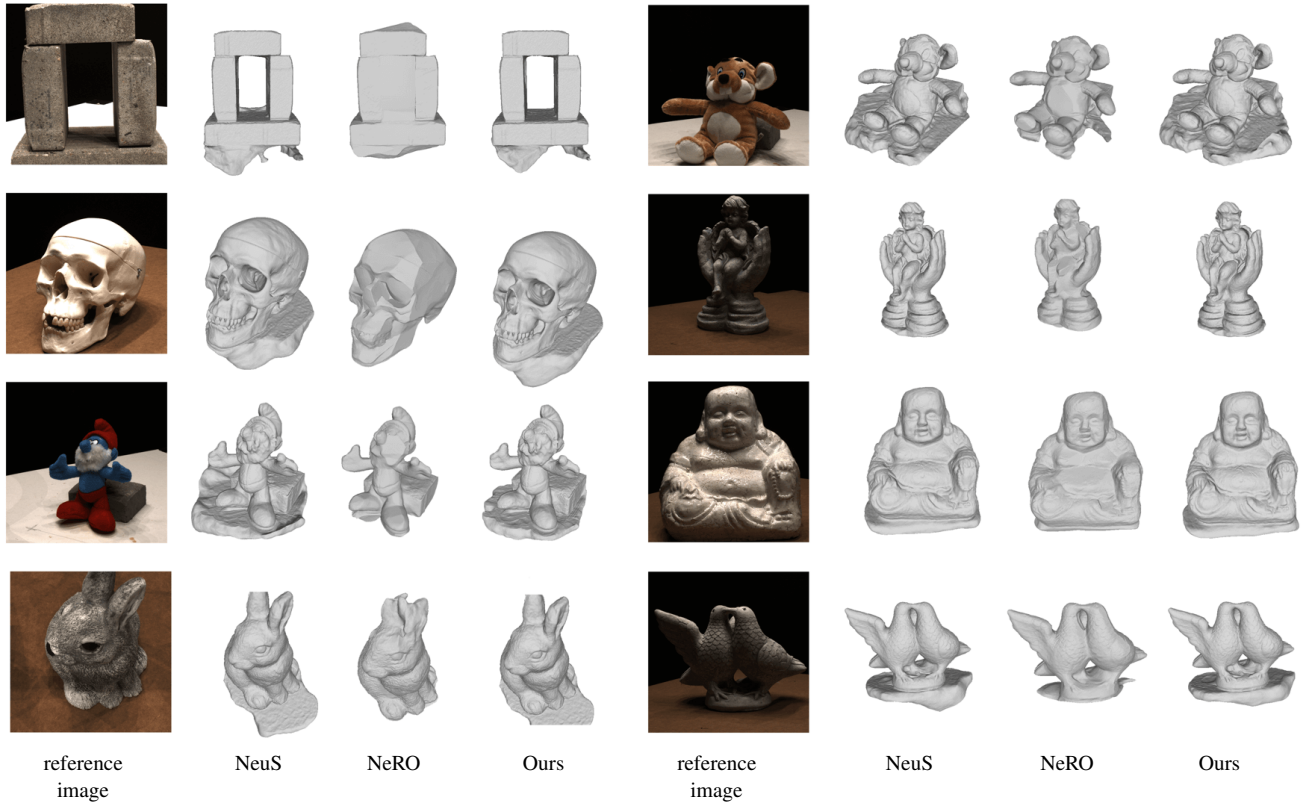


Figure 10. Qualitative results on regular scenes from DTU. with NeRO and NeuS on DTU dataset. Results show that NeRO fails to address the negative impact of partial highlights on the geometry. Moreover, the presence of shadows causes NeRO to mistakenly reconstruct shadowed areas as real objects and fill them in (bricks and skull models).

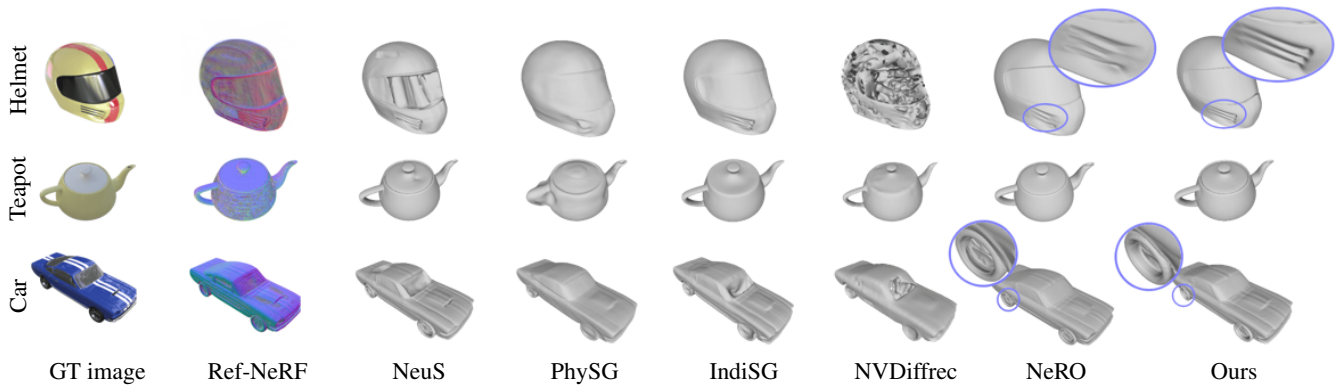


Figure 11. Qualitative results on other scans (helmet, teapot, and car) from the Shiny dataset [39]. NeRO exhibits defects in the dents and highlights of the helmet, as well as in the wheels of the car.

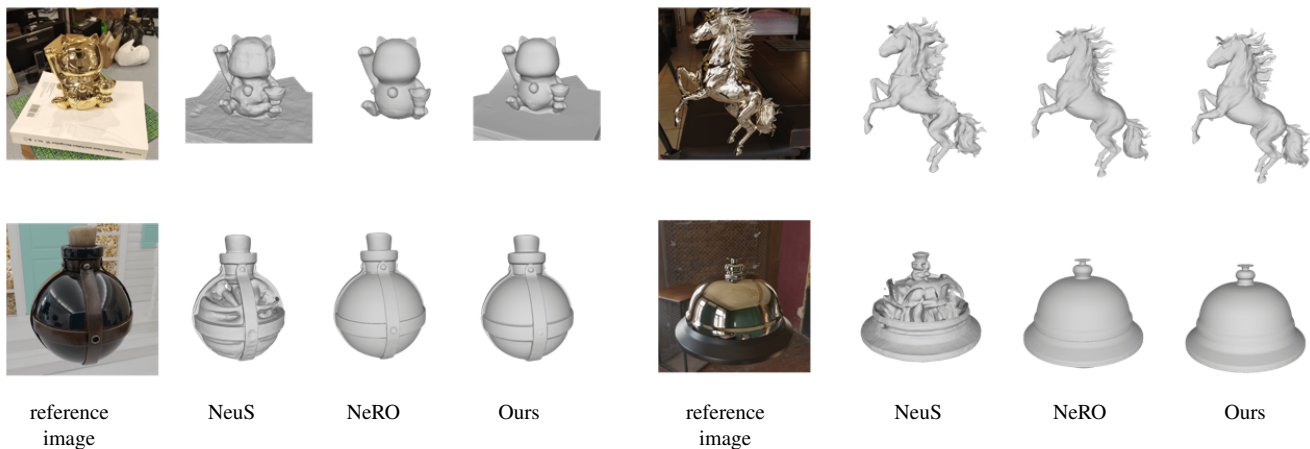


Figure 12. Qualitative results on other scenes (bell, potion, horse, and bell) compared with NeRO and NeuS on the Glossy dataset.

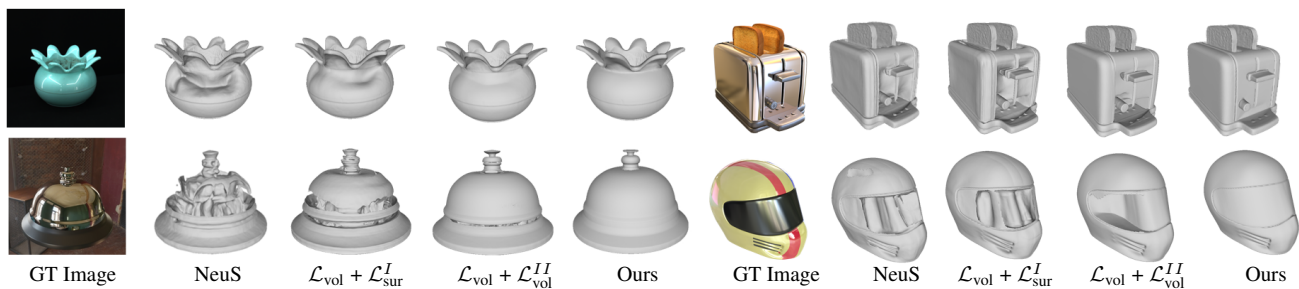


Figure 13. Qualitative ablation evaluation for more objects.



Figure 14. Qualitative comparison with NeRO in terms of material reconstruction and rendering quality.

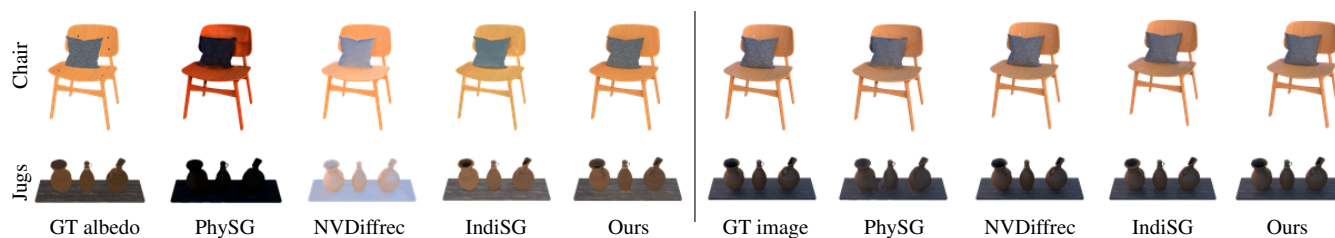


Figure 15. Qualitative results for other scenes (chair and jugs) on IndiSG dataset in terms of albedo reconstruction (left) and novel view synthesis quality (right).



Figure 16. Diffuse and specular decomposition results in the first stage.

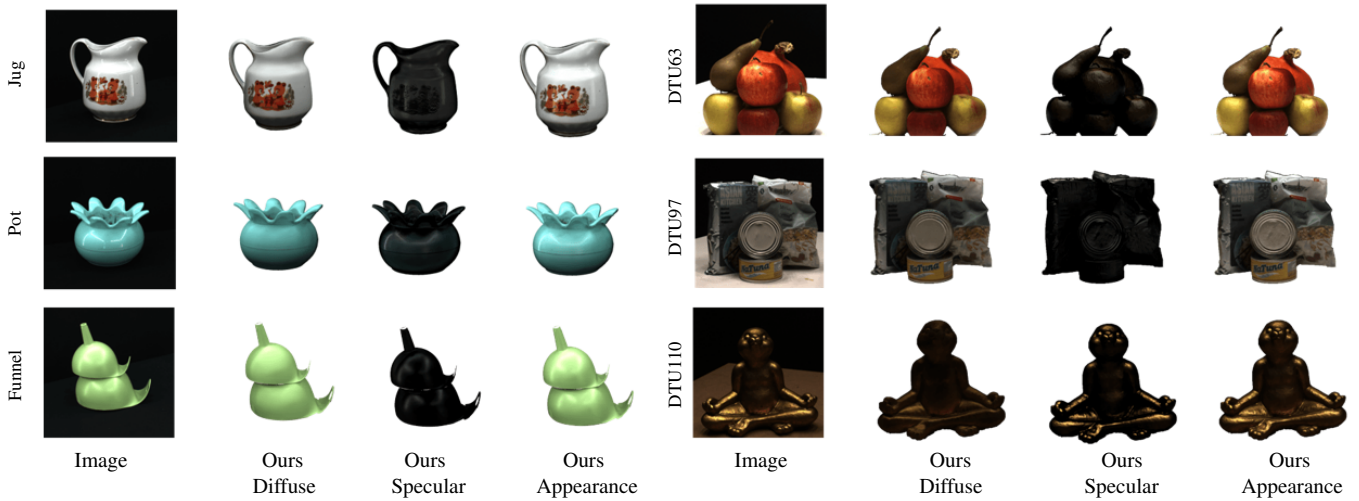


Figure 17. Qualitative results for the SK3D (left) and DTU (right) datasets in the third stage. We can observe that our method can separate the specular reflection component from the diffuse reflection component, as seen in the highlights on the apple, can, and golden rabbit. Even when faced with a higher intensity of specular reflection in SK3D, our method can separate them very well.

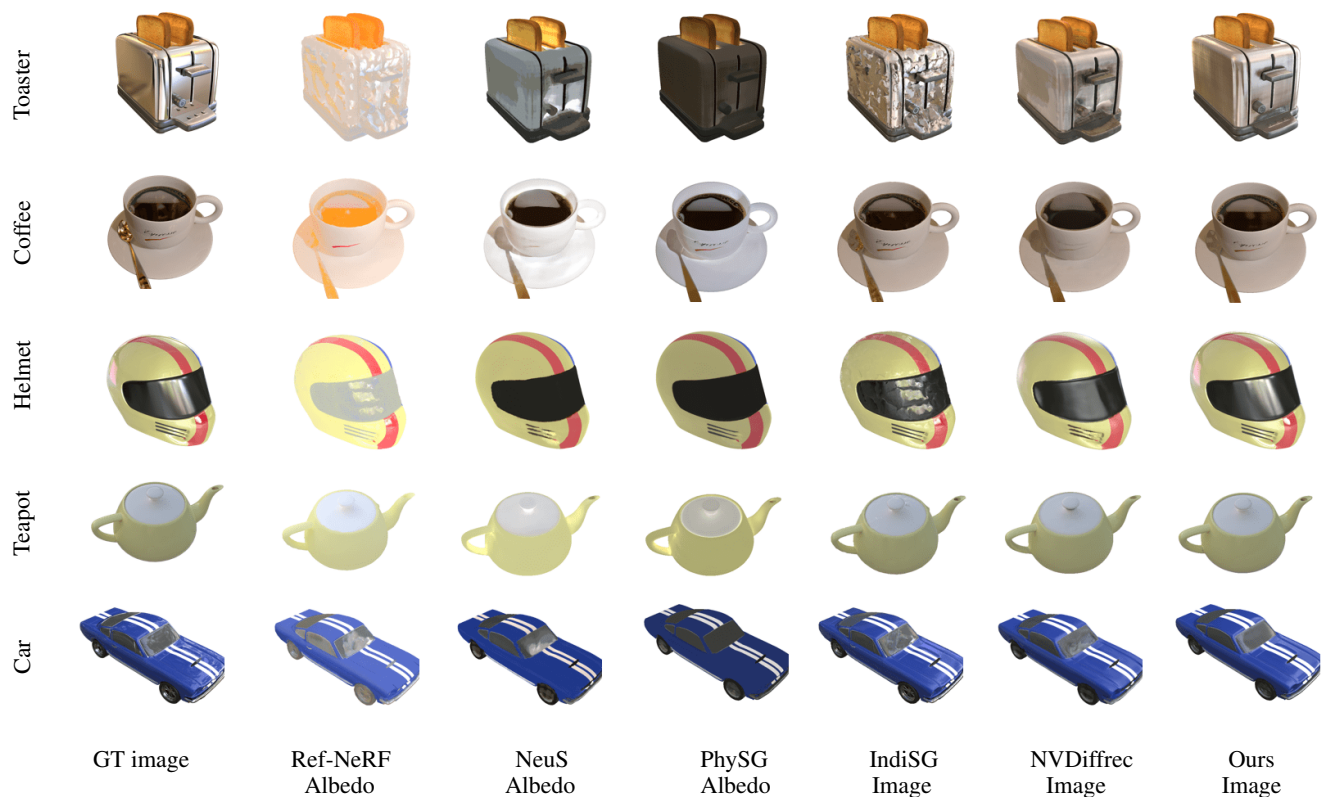


Figure 18. Qualitative results of materials reconstruction for the Shiny dataset, where albedo refers to the diffuse albedo. The results indicate that our method can restore the original appearance with specular highlights more accurately, such as the reflections on the helmet and toaster, and has a better ability to suppress decomposition ambiguity caused by specular highlights.

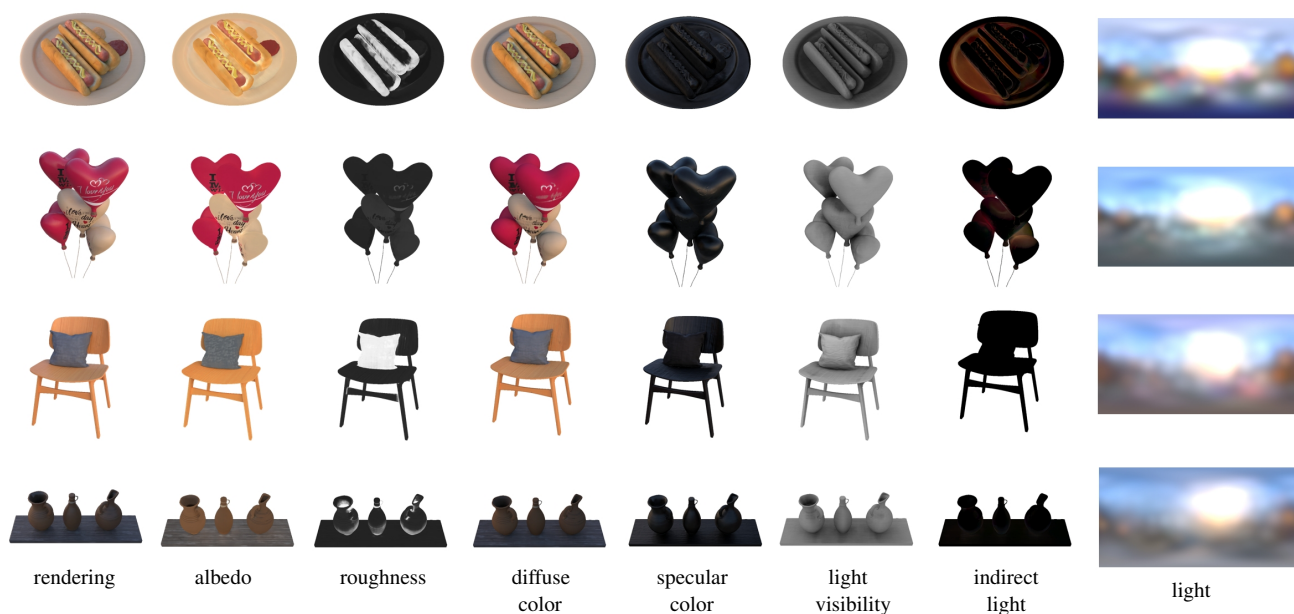


Figure 19. Visualization of all components on IndiSG dataset.

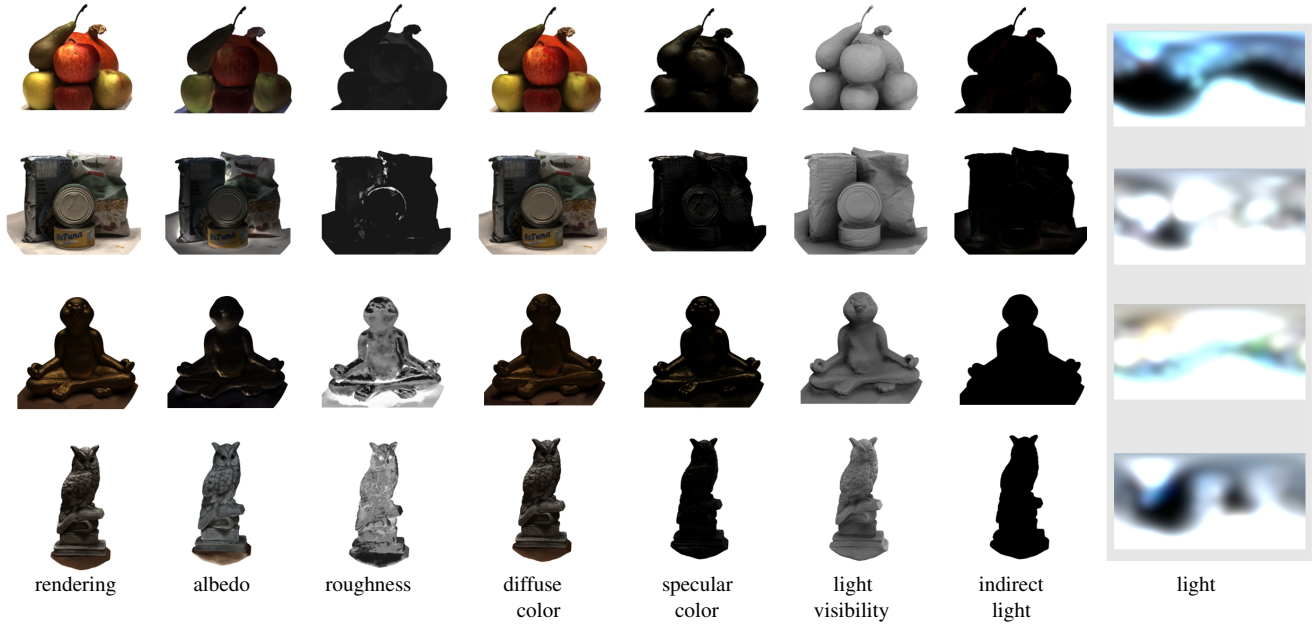


Figure 20. Visualization of all components on DTU dataset.



Figure 21. Visualization of all components on SK3D dataset.

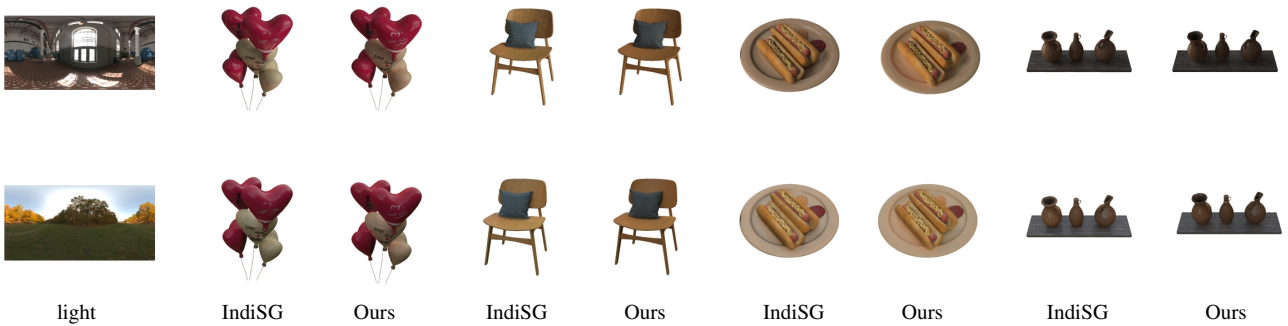


Figure 22. Relighting comparison with IndiSG.



Figure 23. Ablation study of material and illumination reconstruction. We show that introducing specular albedo also makes the sausage appear smoother and closer to its true color roughness, represented by black. In terms of lighting, when not using specular albedo, the lighting reconstruction achieves the best result, indicating a clearer reconstruction of ambient illumination.

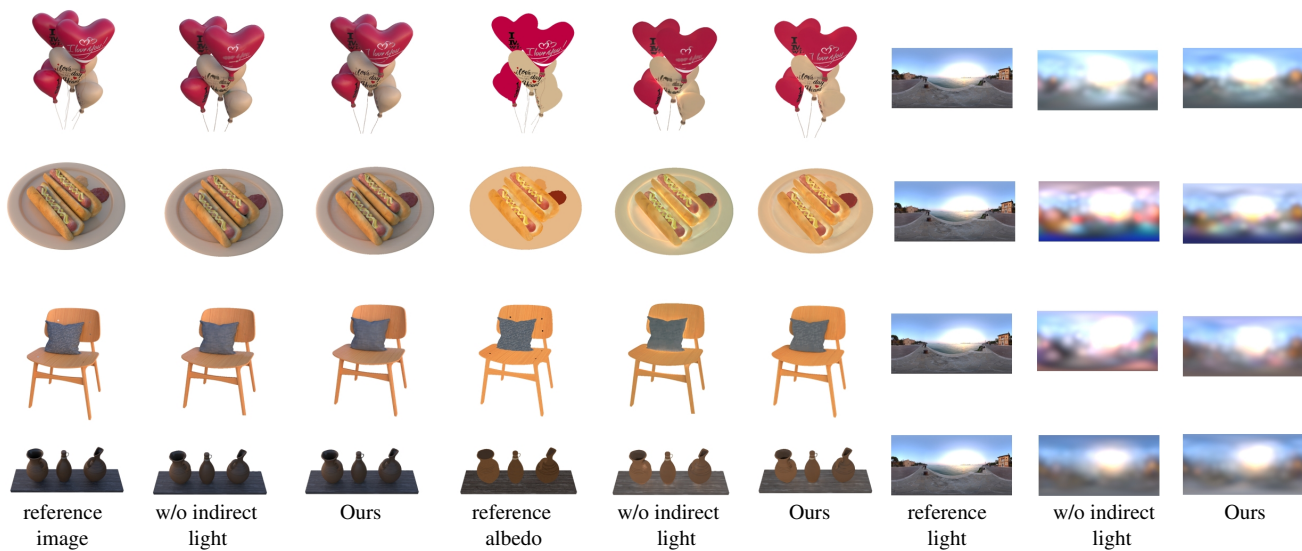


Figure 24. Ablation study of indirect light.



reference
image



Ours
1.15



Ours with Ref-NeRF
2.17



Ours with S³-NeRF
1.23

Figure 25. Comparison with Ref-NeRF and S³-NeRF.



GT image



f=0.02
22.33



f=0.75
24.31



GT image



f=0.02
30.43



f=0.75
30.18

Figure 26. Adjusting Fresnel value to model chrome-like appearance.